ELECTRIC FIELD INDUCED BIREFRINGENCE IN ISOTROPIC SUSPENSIONS OF NANOPLATES

A Thesis

by

JOSE CARLOS MEJIA

Submitted to the Office of Graduate and Professional Studies of
Texas A&M University
in partial fulfillment of the requirements for the degree of

MASTER OF SCIENCE

Chair of Committee,	Zhengdong Cheng
Committee Members,	Svetlana Sukhishvili
	Jodie Lutkenhaus
Head of Department,	Muhammad N Karim

December 2017

Major Subject: Chemical Engineering

ABSTRACT

Isotropic suspensions of colloidal nanoplates are of potential use in electronic displays. Electric field induced-birefringence and the response time of platelets are the two most relevant important properties for display applications. The Kerr coefficient quantifies how high is the field induced-birefringence for a given strength of electric field. The higher the Kerr coefficient, the lower is the required voltage for switching the pixels ON. Therefore, the battery consumption would be lower for high Kerr coefficient platelets. While graphene oxide platelets have shown a potential to be used in displays due to very high Kerr coefficient and very high diameter-to-thickness ratio, a systematic study on the variation of this ratio to study its effect on Kerr coefficient has not yet been done. Very dilute aqueous suspensions of 2D nanoplates of α-zirconium phosphate (α-$Zr(HPO_4)$ abbreviated as α-ZrP) in isotropic phases were tested for electric field induced-birefringence. Different reaction conditions of synthesizing pristine α-ZrP disks in hydrothermal reactor allowed controlled variation of disk sizes. The α-ZrP disks were exfoliated in aqueous medium using tetra-(n)-butyl hydroxide (Bu_4NOH). After exfoliation, nanoplates with uniform thickness (~3 nm) and diameter-to-thickness ratios of 300 to 900 were obtained and then tested for electric field induced-birefringence. The systematic variation in aspect ratio allowed us to study the dependence of Kerr coefficient on nanoplate diameter-to-thickness ratio. The obtained Kerr coefficient of ZrP nanoplates is higher than other platelet systems such as gibbsite, beidellite, but lower than graphene oxide. Due to the shape anisotropy of 2D materials, the electrical polarizability in the plane of this 2D material ($\alpha_{\perp}$) and in the direction perpendicular to

the plane ($\alpha_{\parallel}$) are different. The anisotropy in electric polarizability, defined as $\Delta\alpha = \alpha_{\parallel} - \alpha_{\perp}$, induces birefringence in isotropic samples. The $\Delta\alpha$ value was measured for two different sizes of nanoplates and compared with those predicted by Maxwell-Wagner-O'Konski. By comparing the field interaction parameter of nanoplates for electric and magnetic fields, it turned out that a Tesla of magnetic field and a volt per millimeter of electric field have the same effect in terms of induced-birefringence. Hence, it can be concluded that electric field can easily induce-birefringence in isotropic suspensions of nanoplates as compared to magnetic field.

Dedicated to my beloved grandmother, Teresa, and memory of my grandfather, Ramón, to my parents, Cuco and Miriam, and to my siblings, Eduardo and Paola

ACKNOWLEDGEMENTS

I am extremely grateful to have Dr. Zhengdong Cheng as my academic advisor here at Texas A&M University. He has always been there for me for the past two years; going to his office for discussions; getting scolded in group meetings; attending conferences; but most importantly, he taught me to be a good researcher. We had our ups and downs during my master career, but because of him, I learned to conduct good research, to manage my time, to be myself, and to be more independent. I really doubt I will get to know someone that appreciates or love science as much as Dr. Cheng does. Thank you, Dr. Cheng for your guidance and support in this whole journey. I will never forget it.

There is another person who I would like to acknowledge, to my friend and brother, Abhijeet. He has always been there from the beginning, and he helped me appreciate my research work and finish successfully. I will always appreciate him as a person and all the help that I got from him for the past two years. Thank you very much, Abhijeet. I would also like to acknowledge all my other friends, colleagues, department faculty, and staff for making my time at Texas A&M University a great experience.

Finally, thanks to my loving family for their encouragement and unconditional love. Without their guidance and support, I wouldn't be where I am right now. Thank you, mom and dad.

CONTRIBUTORS AND FUNDING SOURCES

Contributors

Part 1, Faculty Committee Recognition

This work was supervised by a thesis committee consisting of Professor Zhengdong Cheng and Professor Lutkenhaus of the Department of Chemical Engineering and Professor Svetlana Sukhishvili of the Department of Materials Science and Engineering.

Part 2, Student/Collaborator Contributions

All the work for the thesis was completed by the student with the help of Abhijeet Shinde, in collaboration with Dr. Patrick Davidson from the Laboratoire de Physique des Solides in France who provided with small-angle X-ray scattering images of zirconium phosphate nanoplates, Dr. Padetha Tin from NASA Glenn Research Center who provided with the high voltage amplifier, Dr. María Jiménez from the Department of Applied Physics at the University of Granada for giving feedback in the obtained data presented in this thesis, Dr. Mustafa Akbulut from the Department of Chemical Engineering, Texas A&M University, for allowing the use of the Zetasizer instrument from his laboratory, and Dr. Winson Kuo from the Department of Materials Science and Engineering, Texas A&M University, for allowing the use of his FERA3 TESCAN Scanning Electron Microscopy.

Funding Sources

Graduate study was supported for the first one year and half by an assistantship provided by the Department of Chemical Engineering from Texas A&M University. This work was made possible in part by the support from NASA under Grant Number NNX13AQ60G.

NOMENCLATURE

ζ^{-1}	Inverse Aspect Ratio
C_K	Kerr Constant
DC	Direct Current
D_{Disk}	Diameter of Disk
DLS	Dynamic Light Scattering
D_{sphere}	Diameter of Sphere
EBS	Electric Birefringence Spectroscopy
$f(\theta)$	Orientational Distribution of Particles
I-N	Bi-phasic Region
J	Retarder
J'	Quarter Wave Plate
K	Kerr Coefficient
l	Optical Path Length
$L_{\parallel}$	Depolarizing Factor
$L_{\perp}$	Depolarizing Factor
MWO	Maxwell-Wagner-O'Konski
n_e	Extraordinary Ray
n_o	Ordinary Ray
n_s	Solvent Refractive Index
P	Polarizer

PTFE	Polytetrafluorethylene
Q	Bjerrum Length
R	Rotator
S	Nematic Order Parameter
SEM	Scanning Electron Microscopy
TBACl	Tetrabutylammonium Hydroxide
TBAOH	Tetra(*n*-butyl ammonium) hydroxide
TEM	Transmission Electron Microscopy
V_p	Volume of Particle
$ZrOCl_2 \cdot H_2O$	Zirconyl Chloride Octahydrate
ZrP	Zirconium Phosphate
α	(90 – α) to Incident Polarization
δ	Optical Retardation or Phase Difference
Δn	Induced Birefringence
Δn_{eff}	Effective Birefringence
Δn^P	Specific Birefringence
Δn_{sat}	Saturation Induced Birefringence
$\Delta\alpha$	Anisotropy of Polarizability
ε_o	Vacuum Permeability
κ	Debye Length
λ	Wavelength of Light Beam
ρ_{water}	Density of Water

σ	Polydispersity
ϕ	Volume Fraction
ϕ^*	Spinodal Volume Fraction
ϕ_I	Local Volume Fraction
ϕ_{water}	Volume Fraction of Water
ϕ_{ZrP}	Volume Fraction of Zirconium Phosphate

TABLE OF CONTENTS

LIST OF FIGURES

FIGURE Page

FIGURE Page

LIST OF TABLES

CHAPTER I

INTRODUCTION

History of Liquid Crystals

There are three important states of matter – solid, liquid, and gas. A liquid flow and adopts the shape of the container. A solid can be amorphous or crystalline but it cannot flow and tends to keep its shape. Liquids and solids are the two most common condensed matter phases, and the difference is that in solids, the molecules are in order whereas in liquids they are not. The optical properties of both liquids and solids are very different. For example, the polarization of the light changes when it hits a solid but it does not change in liquids. This has brought attention to many researchers and they were interested to see the possibility of the existence of new phases. In the year 1888, a phase transition was observed by an Austrian botanist and chemist, Friedrich Reinitzer[1]. He was observing some esters of cholesterol when he found out two different melting points of the substance. He was doing his experiment with cholesteryl benzoate and noticed that at 145°C, the cholesterol melted from solid to a cloudy liquid. Then when he raised the temperature to 178.5°C, the cholesterol turned into a clear liquid. He also noticed some color changes when the substance was cooling off. He first noticed the appearance of a pale blue color when the clear liquid was turning cloudy then it changed to a bright blue-violet color as the cloudy liquid was crystallizing. He was puzzled with this change that decided to send his samples of this substance to German Physicist Lehmann[2]. The German physicist was specialized to study the crystallization properties of different types of substances. He observed the cholesterol substance under his polarized

microscope and noticed some interesting properties of that sample. He observed that the substance flows like a liquid and contains optical properties the same as in solids. This new investigation was then named *liquid crystals* because it contains both the properties of a solid and a liquid.

The geometrical structure of liquid crystals can be grouped in several types, such as rods[3], disks[4], and bowlic[5]. Liquid crystals that are derived from rod-shaped molecules are called *calamitics*. This type of material has been extensively investigated and it is also very useful for practical investigations. Mesophases of liquid crystals derived from disk-like molecules are called *discotics*. The discotics liquid crystals were not known until late 1970's by scientists Chandrasekhar[4, 6] and Billard[7], and disk-like platelets are still under investigation. The transition of phases in the liquid crystal can be done in two different ways; one way is to be done by thermal processes and the other way is to be done by the influence of solvents. The first method is called *thermotropics* and the second method is called *lyotropics* because one changes phases with temperature and the latter changes phases with concentration. For this investigation, lyotropic liquid crystals of zirconium phosphate platelets are going to be studied because of lack of information in the literature of their electrical properties.

Introduction to External Fields of Liquid Crystals

Liquid crystal is a state of matter that exhibits symmetry intermediate to perfectly ordered crystals and completely disordered liquids. In the past 120 years of liquid crystal research, more than 800 thousand molecular liquid crystal systems are characterized whereas less than fifty colloidal particulate suspensions are reported to show liquid crystalline phases. Liquid crystals of 2D colloidal particles, which are particles from the range of 1 nm to 10 μm, are of emerging research interest[8]. External electric field influences the microstructural ordering within nanoplate liquid crystal, and there have only been a couple of efforts[8-9] in this research direction. They demonstrated that shape anisotropy of nanoplates leads to electric polarization anisotropy in the system[10].

There has been many missing literature in exfoliated zirconium phosphate in its electrical properties, and the goal of this project is to fill the missing gaps of the important properties of this 2D colloidal suspension. Some interesting properties of α-zirconium phosphate is that they are monodisperse, controllable aspect ratio, and biodegradable[11]. The Onsanger's theory predicts the transition from isotropic to nematic phase, which passes through a biphasic region[12]. The location of the phase transition widely depends on the aspect ratio of the platelet and can be perfectly described in phase diagrams.

Quadratic electro-optic effect, also known as the Kerr effect, quantifies induced birefringence due to the application of electric field in which the birefringence originates from the alignment of nanoplates. This effect is induced in colloidal systems when an electric field is applied. The induced birefringence is the difference between the

refractive index parallel and perpendicular to the electric field[13]. The difference in the two rays describes the anisotropy of their orientation distributions as the electric field exerts a torque to the platelets[14]. The Kerr effect is a fundamental study that explains the transition between isotropy to anisotropy[15-16]; in other words, it is when the suspension shows birefringence in response to an external stimulus. The DC component of the induced birefringence, Δn_{DC}, can provide fundamental understanding of the electrical field[17-18]. In the Kerr effect theory, the induced birefringence is linearly proportional to the square of the electric field. As the field is increased, the induced birefringence cannot longer increase; this is when the signal saturates and platelets show perfect orientation alignment.

The goal is to compare the Kerr coefficient of exfoliated zirconium phosphate platelets to other systems. In previous studies, it has been demonstrated that the Kerr coefficient of graphene oxide is approximately 1.8×10^{-5} m/V^2 and claimed that their Kerr coefficient is the largest compared to other colloidal materials[10, 19]. There are also previous studies that measures the Kerr coefficient of 2D Gibbsite platelets, which is in the order of magnitude of 10^{-9} m/V^2.[17] Another type of liquid crystal is the polymer-stabilized blue phase which is the next-generation display technology due to its high Kerr coefficient of magnitude between 10^{-8} to 10^{-9} m/V^2.[10, 20] In conclusion, the application of external fields is of prime importance for fundamental studies and possible development of liquid-crystal devices.

CHAPTER II

ZIRCONIUM PHOSPHATE PLATELETS

The synthesis of crystals with high anisotropy shapes through innovated chemical methods has been studied over a century now. Disk-like nanoplates have been found in various applications such as discotic liquid crystals[8, 21-23], Pickering emulsions[24-26], and functional membranes[27]. Some of the key factors in the applications of disk-like nanoparticles are the shape, size polydispersity, orientational order, and number density[28]. Previous studies, both experimental and theoretical, have shown that in discotic liquid crystals, for instance, the self-assembling of platelets dispersed in a solvent is very sensitive in the geometric factors of the particles[29-30]. A well-known form of crystalline acids of zirconium is the α-zirconium phosphate. Zirconium phosphate platelets have been found in many applications as artificial kidneys[31], membranes for direct methanol fuel cells[32], and as modified Janus nanoplates for drug delivery which it is still being conducted in the laboratory. In the production of α-ZrP crystals, van der Wall forces between layers take place, as well as covalent bonds between atoms in each layer and hydrogen bonding[33]. α-ZrP crystals can be synthesized in many forms, such as reflux method[34], hydrothermal method, [11, 35], and microwave-assisted synthesis method[36]. In this study, the disk-like ZrP are going to be synthesized using the hydrothermal method because of the effective control in size, thickness, aspect ratio, and polydispersity[11]. In addition to the controllable of size, α-ZrP has several advantages over natural clay, such as high ionic exchange[37-38] and ease intercalation and exfoliation[39].

As mentioned before, the alpha-zirconium phosphate platelets were synthesized via the hydrothermal method due to the following reasons. Hydrothermal method provides high inverse aspect ratio and the size distribution is in the range of 35-40%. The fact that the platelets were not synthesized using the reflux method is because of the difficulty to obtain very large platelet size. However, the microwave-assisted method provides even higher platelet size compared to the hydrothermal method but the size distribution is very wide.[34, 39] There has not been any reported data in the maximum particle size length. However, in our lab, the largest synthesized particle size was about 2342 nm, which has not been reported in the literature. There are no particle size limits as of now, but as the concentration of phosphoric acid increases, as well as the reaction time in the oven, the particle increases in size accordingly.

Synthesis of α-Zirconium Phosphate Platelets

6 grams of zirconyl chloride octahydrate ($ZrOCl_2 \cdot H_2O$, 98+%, Acros Organics) and 60mL of phosphoric acid (85%, certified CAS, Fisher) were used to synthesize the α-ZrP disks. This procedure was done by using the hydrothermal method[11, 35]. In two different centrifuge tubes, 3 grams of zirconyl chloride octahydrate was added in each tube. Then, 30 mL of 15 M of phosphoric acid was added to the zirconyl chloride octahydrate powder in each tube. The reason that it was done in two different centrifuge tubes is because the solution should be completely homogenized. Afterwards, the sample was vortexed until it became well-mixed and a gel-like mixture was seen. The resulting mixture was then poured into a 20 mL PTFE container and placed in an autoclave. Once

the autoclave is completely secured, it should be kept in an oven at 200°C for various lengths of time. For this experiment, two different autoclave containers were kept in the oven at two different interval times: one for 8 hours and the other for 316 hours. The size of the particle is dependent on the time that the system is in the oven. After the desired time has been achieved, the autoclave was allowed to cool down in room temperature for about 8 hours under ambient conditions. In this entire synthesis of α-ZrP disks, the chemical reaction that took place was

$$ZrOCl_2.8H_2O + 2H_3PO_4 \rightarrow Zr(HPO_4)_2.H_2O + 2HCl + 8H_2O$$

After the autoclave has been cooled down, the PTFE container was removed from the autoclave and only the resulting α-ZrP disks were collected by centrifugation. The disks were then washed with distilled water under centrifugation three times. After washing, the sample was then dried in an oven at 64°C overnight. The dried sample was then ground with a mortar and pestle into fine powder as shown in **Figure 1**.

Figure 1. Final product of α-ZrP disks.

The resulting α-ZrP disks were characterized under scanning electron microscopy (FERA3 TESCAN) operated at 10 kV, working distance of 9 mm, at different magnifications. Since the disks are not very conductive, the sample was coated with 5 nm of Pt/Pd for better image processing. The SEM analysis was mainly used to study the morphology characterization of the platelets, as well as the shape of the disks, their roughness, and the distribution of sizes. As explained before, two different sizes of platelets were synthesized using hydrothermal method and the SEM image can be seen in **Figure 2** and **Figure 3**. Also, the crystallinity of the nanoplate increases as the reaction time increases, as it can be seen in the SEM images.

There is a three-stage growth of α-ZrP disks that describes the formation of the crystals under the hydrothermal method. The first stage involves the formation of ZrP crystalline nuclei. In the second stage, the crystals get attached into one another, and the attachment happens due to the formation of hydrogen bonds into the flat surface of the disk, <001> plane. During the third stage, all the small crystals fuse into the big crystals forming one single multi-layer crystal, and all the defects get repaired through the Oswald ripening. However, the sample will be polydisperse but it can be controlled by adding some capping agents which can control the shape of the crystals, making it more monodisperse.[11]

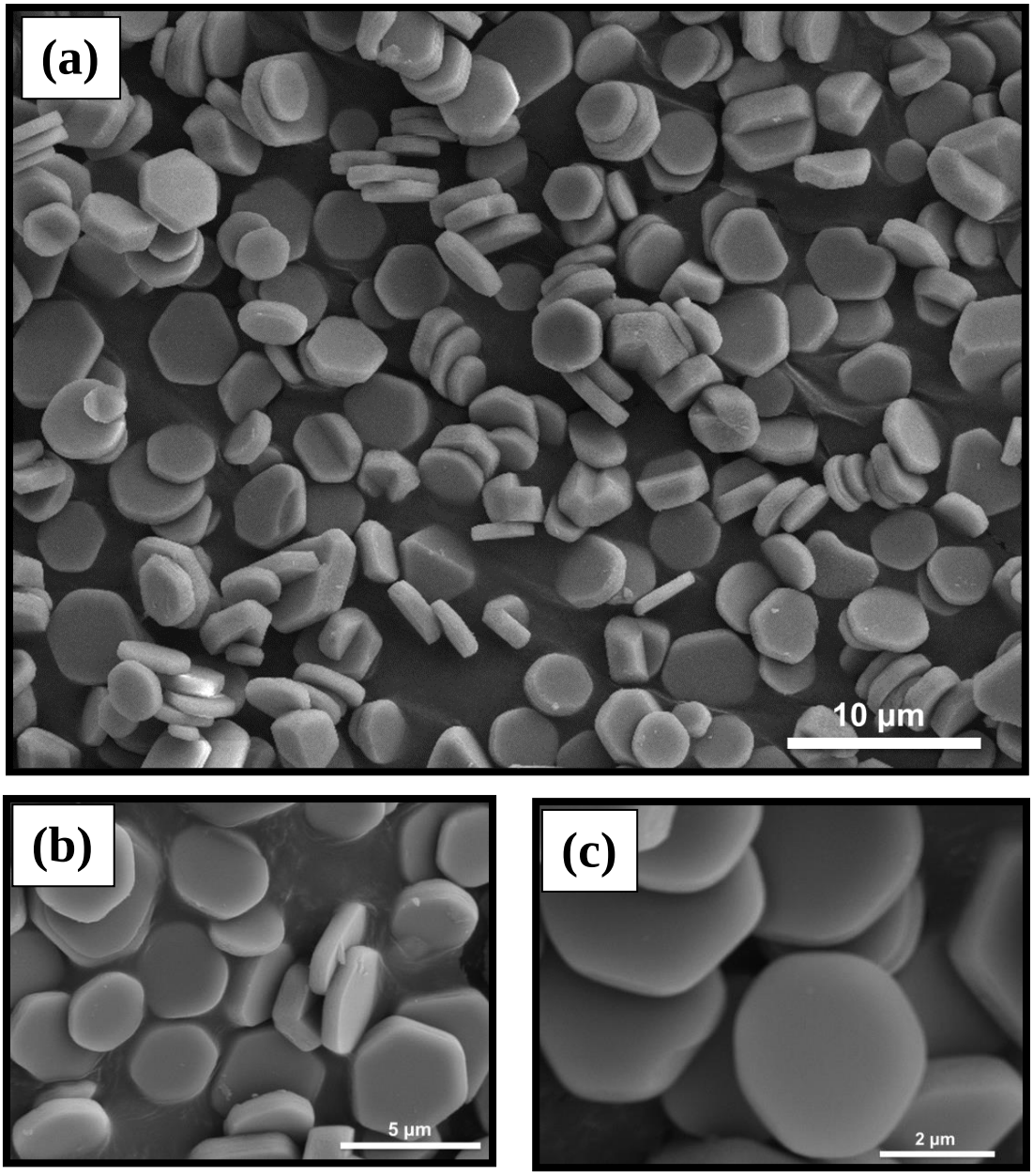

Figure 2. SEM image of synthesized α-ZrP disks in 15 M phosphoric acid for 316 hours at different magnifications. (a) 5.00 kx, (b) 12 kx, (c) 25 kx.

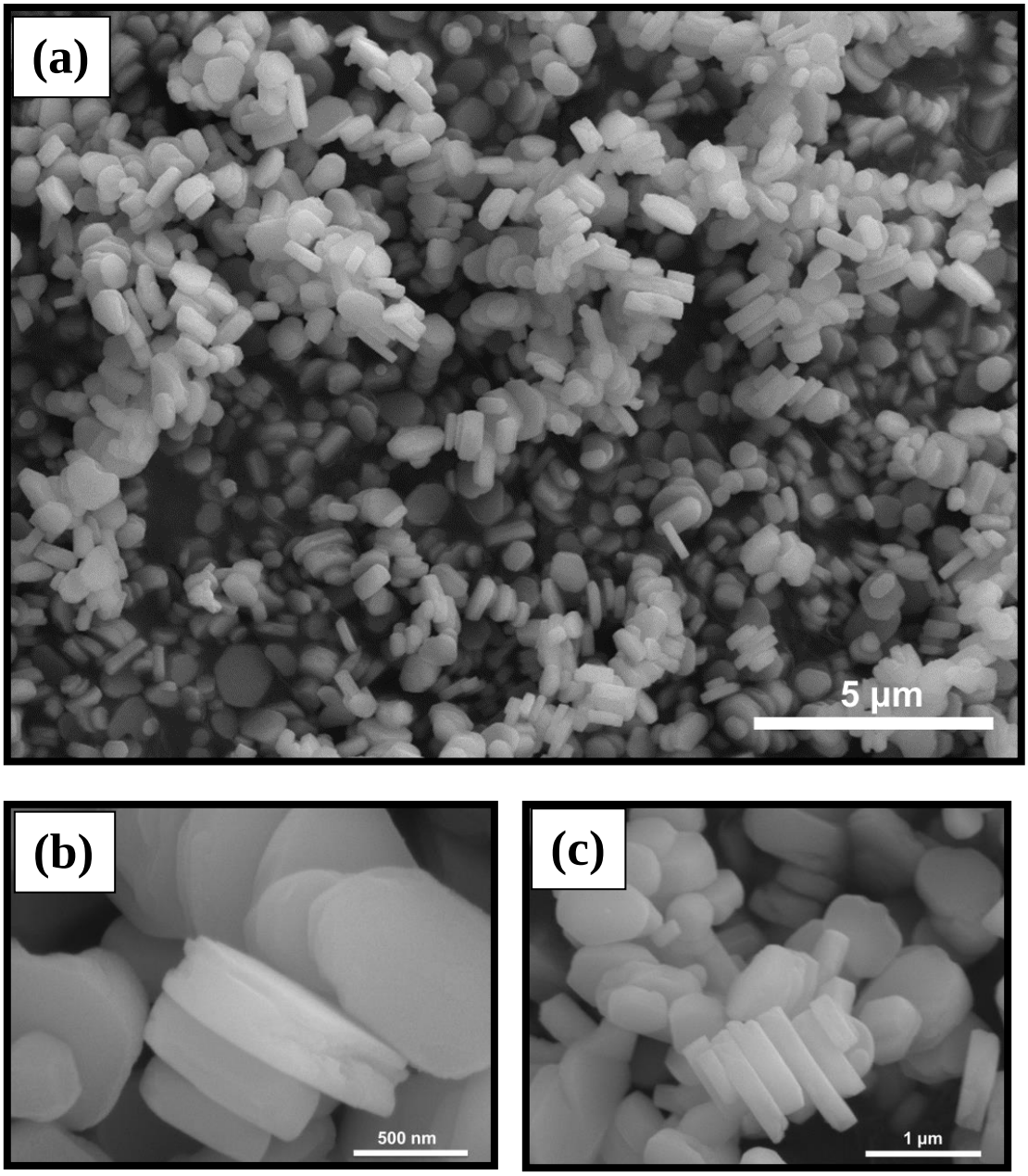

Figure 3. SEM image of synthesized α-ZrP disks in 15 M phosphoric acid for 8 hours at different magnifications. (a) 10 kx, (b) 100 kx, (c) 50 kx.

From the SEM images, it is seen that the platelets are hexagonal in shape, they have uniform thickness, but the polydispersity is very high. The dispersity of the sample

depends on several factors, such as the formation of the nucleus. The polydispersity of the sample can be improved if the formation of the nucleus is uniform. This can be controlled by making sure that the sample is well-mixed before loading it into the PTFE container and placing it into the oven. Also, the reduction of particle's polydispersity can be achieved by fractionation[40]. Using ImageJ (v1.44p, National Institutes of Health), the size of each disk can be obtained but very rigorous to determine the size distribution of the platelets (polydispersity); therefore, another method, dynamic light scattering (DLS), was used to measure the average size and size distribution, which will be explained later.

Exfoliation of Zirconium Phosphate Platelets

In order to obtain monolayers of ZrP of uniform thickness, the multilayered crystals were exfoliated by dissolving the crystal 7.8 mL of Milli-Q water and subsequently adding 2.2 mL of tetra(*n*-butyl ammonium) hydroxide (TBA^+OH^-, Sigma-Aldrich, 40% water) drop by drop at a molar ratio of 1:1 ZrP: TBA^+OH^- at room temperature. After the exfoliation, the suspension was treated under sonication for about 30 to 60 minutes and were put in rest for 3 days to ensure full intercalation of the TBA and complete exfoliation of ZrP[29, 41]. The schematic exfoliation process and structure of zirconium phosphate crystals with exfoliation are shown in **Figure 4** and **Figure 5**.

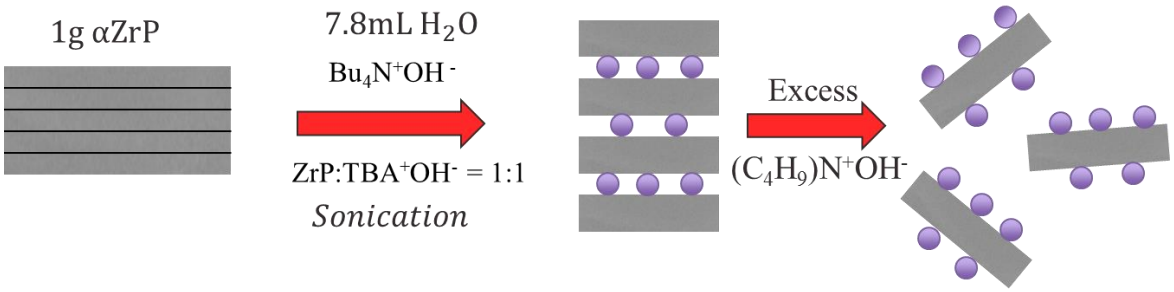

Figure 4. Exfoliation of α-ZrP going through exfoliation by using excess of TBA. The purple circles around the monolayers are TBA^+. The obtained monolayer has thickness of 26.8 Å.

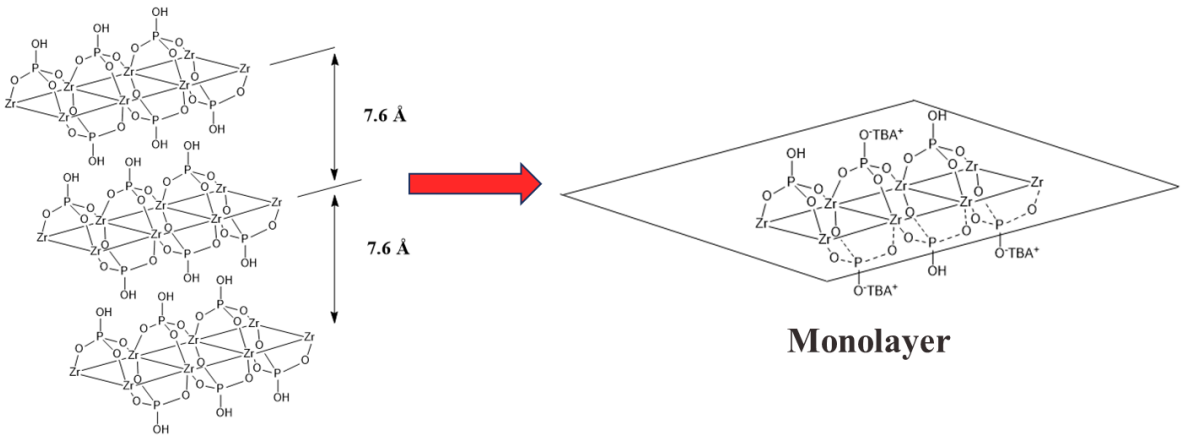

Figure 5. Structure of crystalline multilayer ZrP before exfoliation and structure of monolayer ZrP after exfoliation.

Transmission electron microscopy (TEM) (FEI Tecnai G2 F20 FE-TEM) image of the small platelets are shown in **Figure 6**. From the TEM image, it can be seen that the platelet got fully exfoliated and retained its shape.

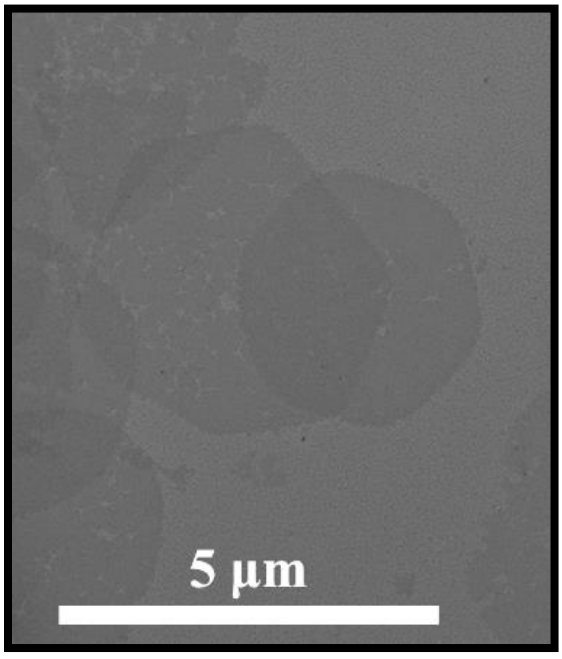

Figure 6. Transmission Electron Microscopy (TEM) image of exfoliated ZrP in 15 M phosphoric acid concentration of 316 hour under hydrothermal treatment.

The size and polydispersity of the sample were calculated using a dynamic light scattering (DLS) (Zetasizer Nano ZS). DLS makes measurements assuming that the platelets are spheres in shape but this is not the case. The measurements gathered from the DLS need to be converted into the actual diameter of the disk. The following conversation was used to measure the actual diameter of the disk:

$$D_{sphere} \tan^{-1}\left(\sqrt{\frac{{D_{disk}}^2}{t^2} - 1}\right) = t\sqrt{\frac{{D_{disk}}^2}{t^2} - 1}$$

where D_{sphere} and D_{disk} are the diameter of the sphere measured in DLS and the actual diameter of the disk, respectively, and *t* is the thickness of the disk[42]. The actual diameter of the disk was obtained by iteration since the diameter of the sphere and the thickness of the disk are known. The size distribution for both the large platelets and small platelets are plotted using OriginPro 8.5 in **Figure 7** and **Figure 8**. It was calculated that the size distribution of the large platelets is 2343 ± 1181 nm, and for small platelets, the size distribution is 753 ± 357 nm. The polydispersity (σ) of the suspension was calculated by taking the ratio of the standard deviation and the mean.

$$\sigma = \frac{\sqrt{variance}}{mean}$$

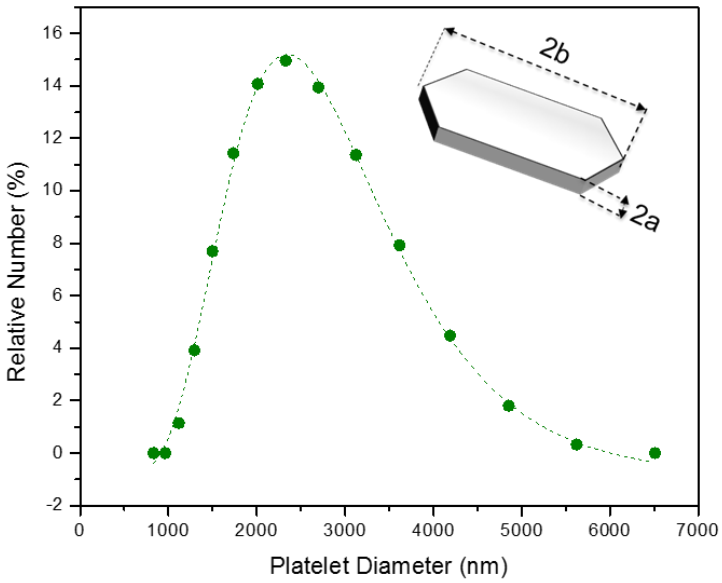

Figure 7. Size distribution of large platelets using DLS and converted into actual diameter. The platelet diameter was calculated as 2343 ± 1181 nm with polydispersity of 40.25% and mean of 2935.02.

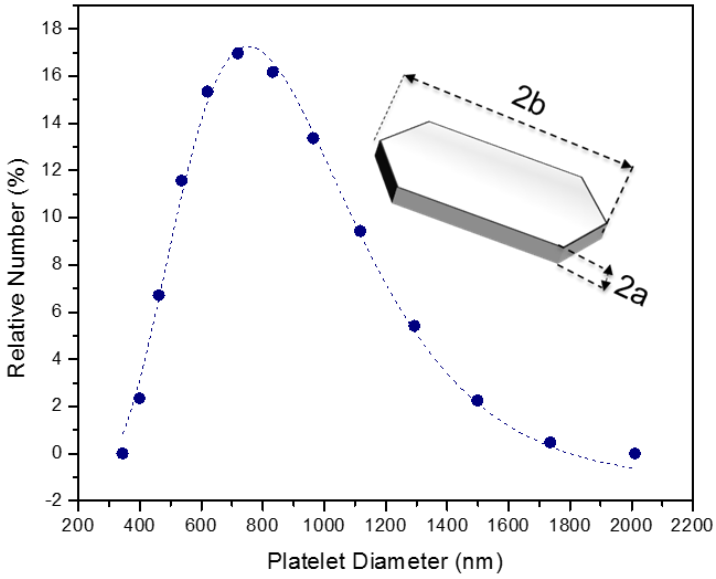

Figure 8. Size distribution of small platelets using DLS and converted into actual diameter. The platelet diameter was calculated as 753 ± 357 nm with polydispersity of 38.49% and mean of 925.91.

Liquid Crystals Phase Diagrams

Using the Onsager's second virial theory[43], Wensink *et al* studied the hard-colloidal platelet phase diagram for different aspect ratios[44]. The phase diagrams give available information on the phase transitions of the system as the volume fraction is increasing. The Onsager theory predicted that for anisotropy colloidal platelets with small aspect ratio (thickness/diameter), the nematic phase forms at a lower volume fraction[45]. For lyotropic liquid crystals, the disk-like platelets change phases with increasing concentration, from isotropic, to nematic[46], to smectic 1D, to columnar 2D[47], and finally to crystal 3D as shown in **Figure 9**.[48]

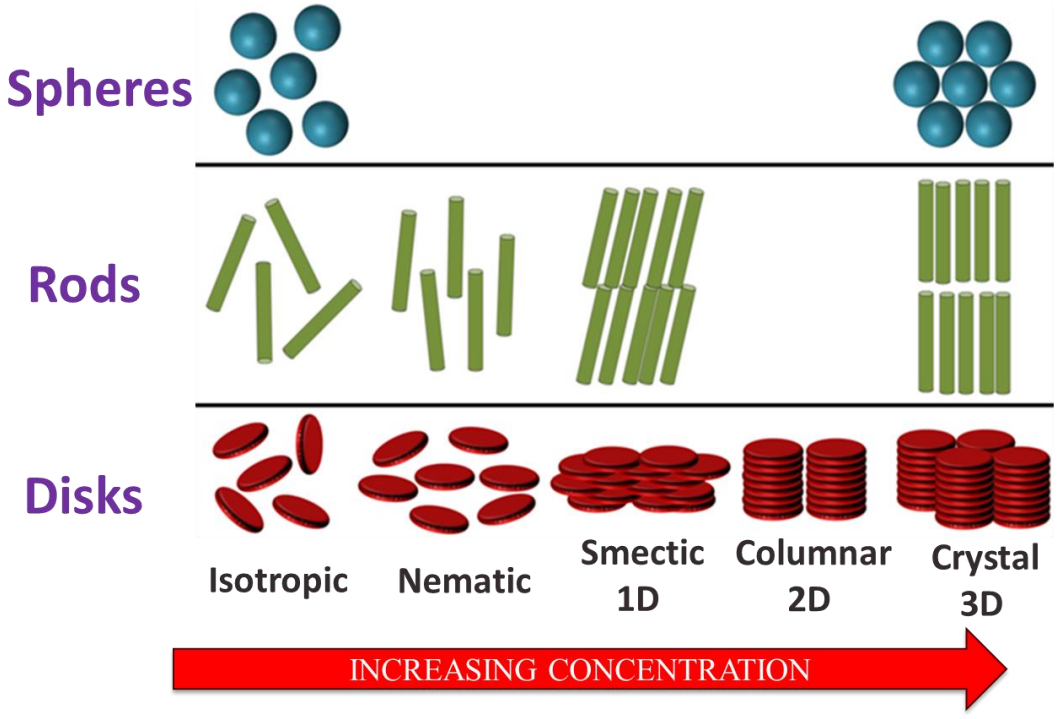

Figure 9. Representation of lyotropic liquid crystal phases in increasing concentration for spheres, rods, and disks.

The phase diagrams were first obtained by calculating the volume fraction of the mother suspension. The volume fraction of ZrP was calculated by adding 1 mL of the mother suspension to a Petri dish and then removing all the water out in a vacuum. After all the water has been dried out from the suspension in the Petri dish, the volume fraction was calculated by using the following expression,

$$\phi_{ZrP} = 1 - \phi_{Water} = 1 - \left\{ \frac{\left\{ \frac{W_o - W_d}{\rho_{water}} \right\}}{1\ mL} \right\}$$

where W_o is the weight of the suspension before drying, W_d is the weight of the suspension after drying, and ρ_{water} is the density of the solvent, which is water. After the volume fraction has been obtained, then the suspension can be diluted to different concentrations to form a phase diagram as shown in **Figure 10**.

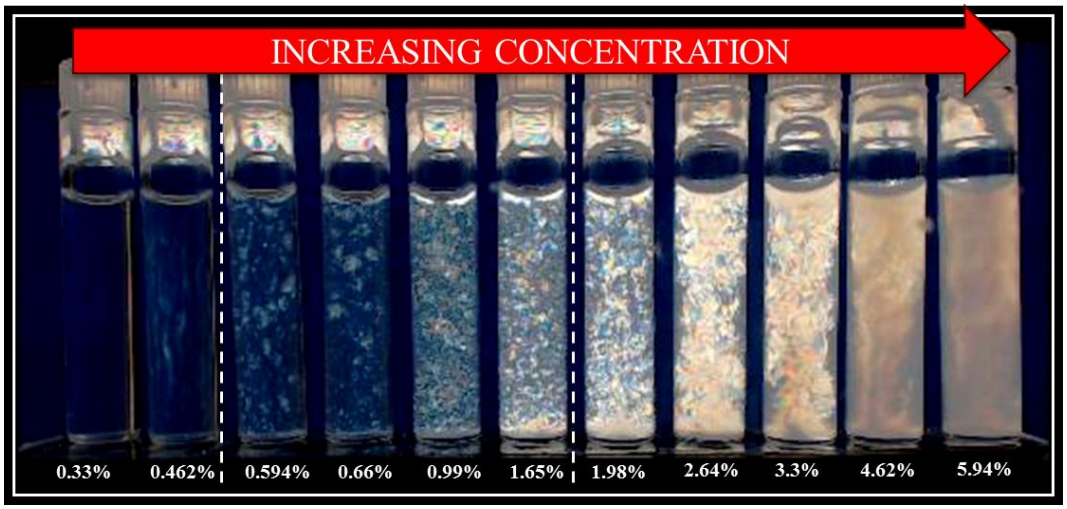

Figure 10. Phase diagram of large platelets of inverse aspect ratio of 901 ± 454. This is at onset. The samples between the dashed lines are in the biphasic (I-N) transition. The sample before volume fraction of 0.462% is in isotropic region and after 1.98% is in full nematic.

The following figure, **Figure 11**, shows snapshots of suspension of average nanoplate size of 2343 nm and a nanoplate volume fraction of $\phi = 6.6\%$ at three different times. The suspension was diluted into 11 different concentrations. At onset ($t = 0$), the suspension was homogenized by flipping the vial up and down while making sure that there are no bubbles trapped inside the suspension. The suspensions were then put to rest while taking pictures every two hours using a CCD camera for continuous 25 days. It can be seen from the figure that the suspension underwent nucleation of nematic crystalline, also known as tactoids[49], in matter of minutes as well as sedimentation due to gravity. After all the nematic tactoids settled down to the bottom of the vial, a clear interface can be seen which distinguishes between isotropic and nematic phase. For larger platelets, it took about 25 days for all the nematic tactoids to sediment to the bottom of the vial. The nematic fraction equilibrium as a function of volume fraction for larger platelets is shown in **Figure 12**. The equilibrium phase diagram was obtained by measuring the height of the birefringent nematic phase of the sample every two hours until complete sedimentation has occurred. Afterwards, the height of the birefringent nematic phase was plotted as a function of time for only one concentration. This was also done for other concentrations. Then, the data points were fitted into a linear fit with negative slope because the height of the birefringent phase decreases with time. The birefringent height as a function of time for one concentration was then interpolated as time goes to zero, and the nematic phase equilibrium for that concentration was obtained. This value tells nematic fraction of the system under no sedimentation, *i.e.* no gravity.

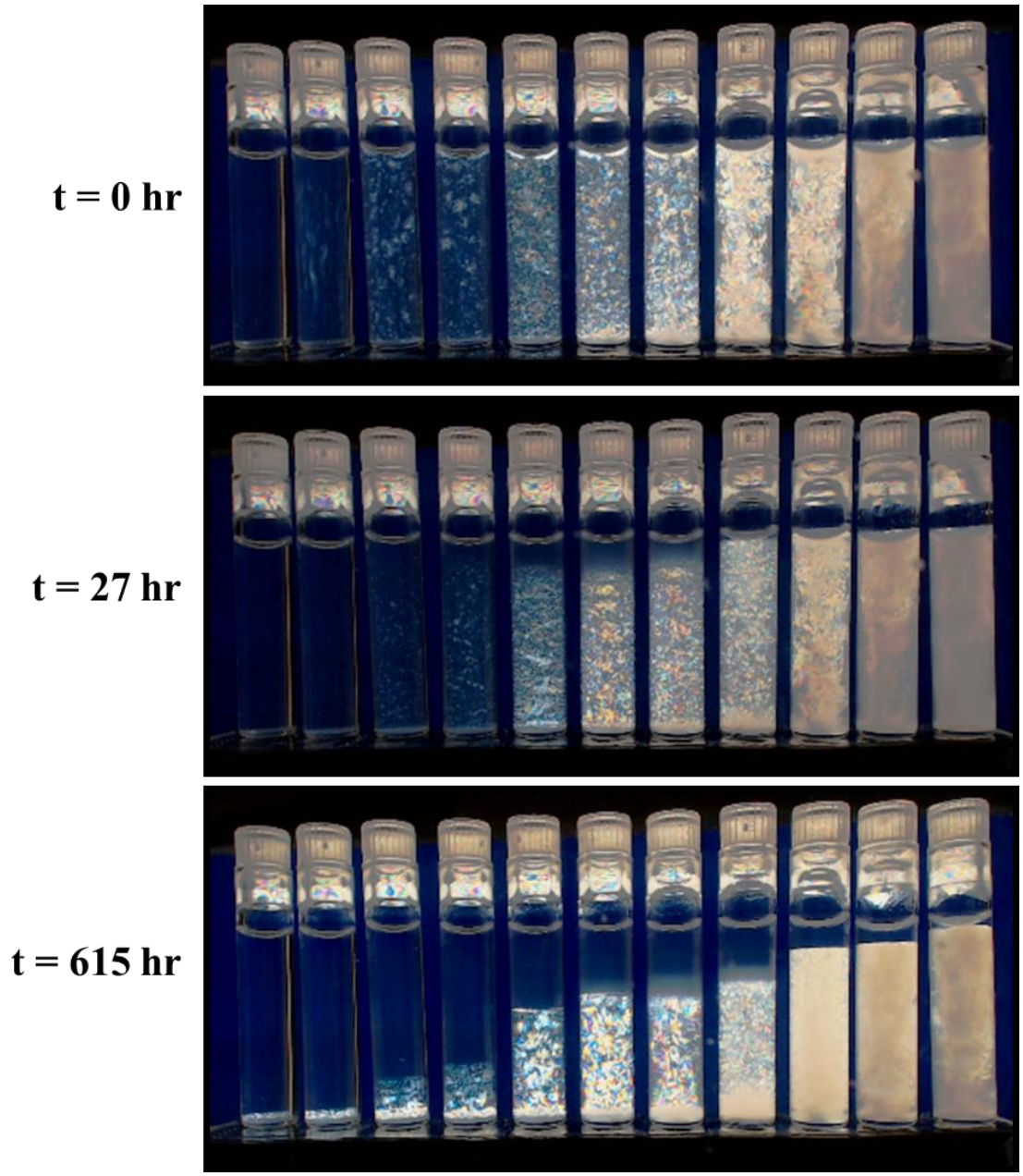

Figure 11. Snapshots of nanoplate suspension of inverse aspect ratio of 901 ± 454 between crossed polarizers with a ZrP volume fraction of $\phi = 6.6\%$ at three different times, beginning (t = 0), intermediate (t = 27 hr), final (t = 615 hr). Left to right, ϕ = 0.0033, 0.00462, 0.00594, 0.0066, 0.0099, 0.0165, 0.0198, 0.0264, 0.033, 0.0594.

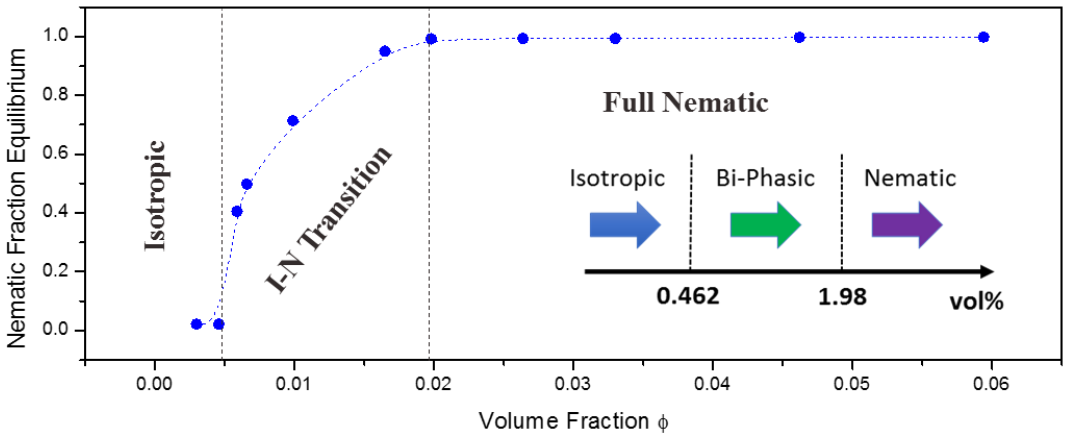

Figure 12. Fraction of nematic phase as a function of volume fraction for large platelets. The phase diagram is divided into three regions: isotropic, I-N, and nematic.

The same work was done for the smaller platelets with size of 753 ± 357. The concentrations used for this phase diagram are shown in **Figure 13**.

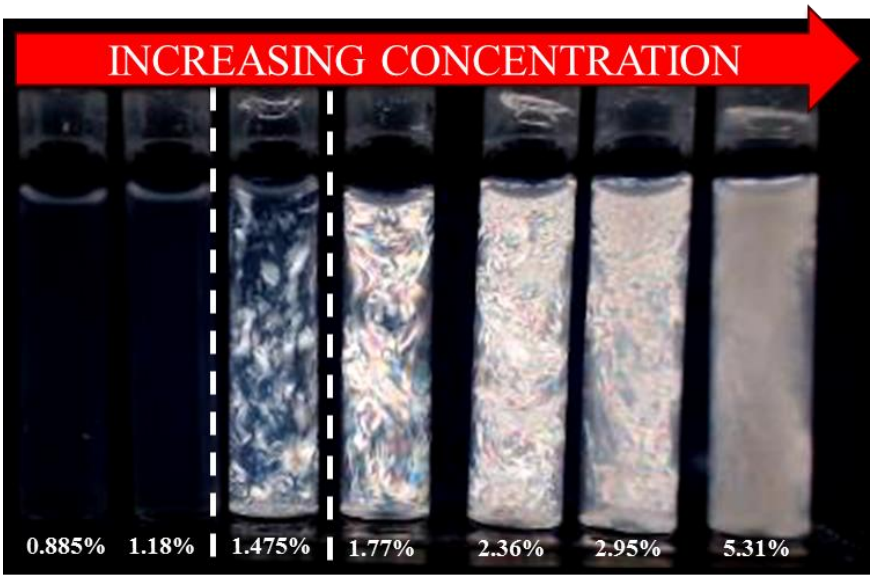

Figure 13. Phase diagram of small platelets of inverse aspect ratio of 290 ± 137. This is at onset. The sample between the dashed lines is in the biphasic (I-N) transition. The sample before volume fraction of 1.475% is in isotropic region and after in full nematic.

The following figure, **Figure 14**, shows a complete phase diagram for small platelets.

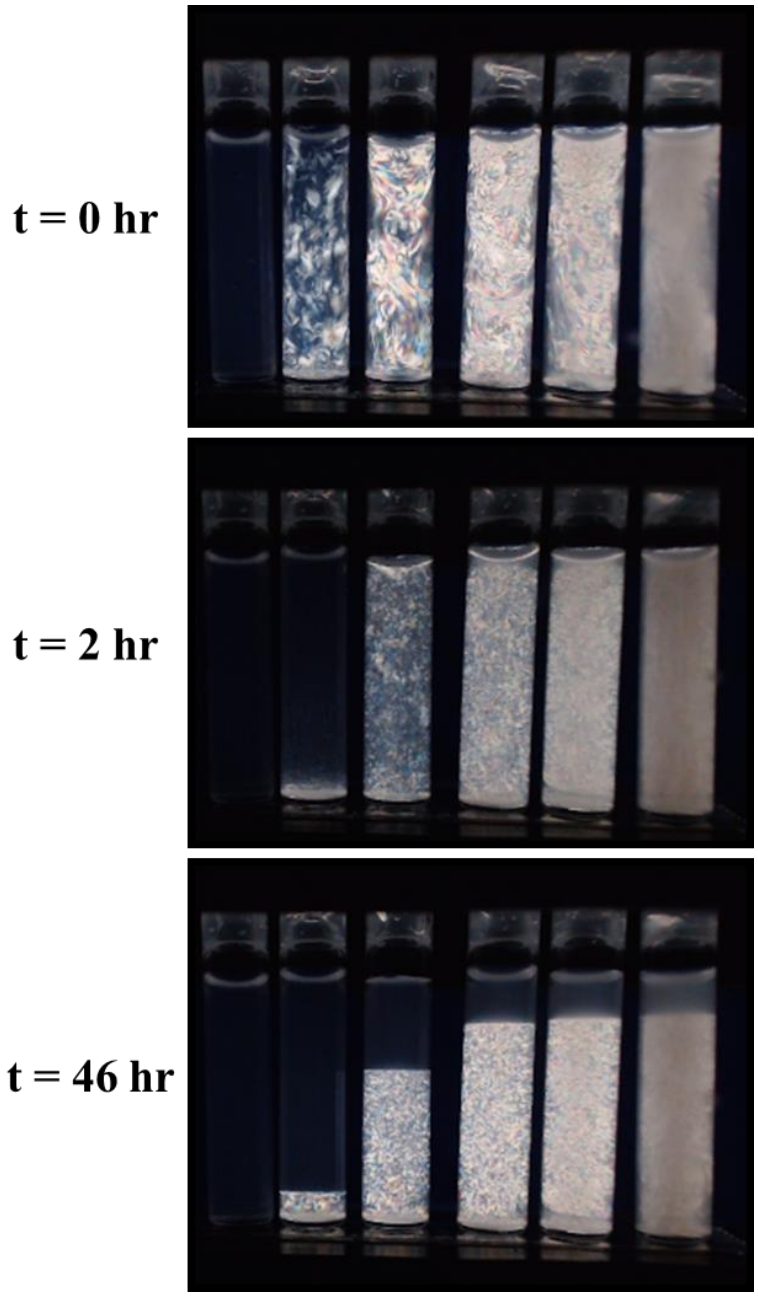

Figure 14. Snapshots of nanoplate suspension of inverse aspect ratio of 290 ± 137 between crossed polarizers with a ZrP volume fraction of $\phi = 5.9\%$ at three different times, beginning (t = 0), intermediate (t = 2 hr), final (t = 46 hr). Left to right, ϕ = 0.00885, 0.0118, 0.01475, 0.0177, 0.0236, 0.0295, 0.0531.

The nematic fraction was also plotted for small platelets, as shown in **Figure 15**, and the procedure to obtain the data is the same as for large platelets.

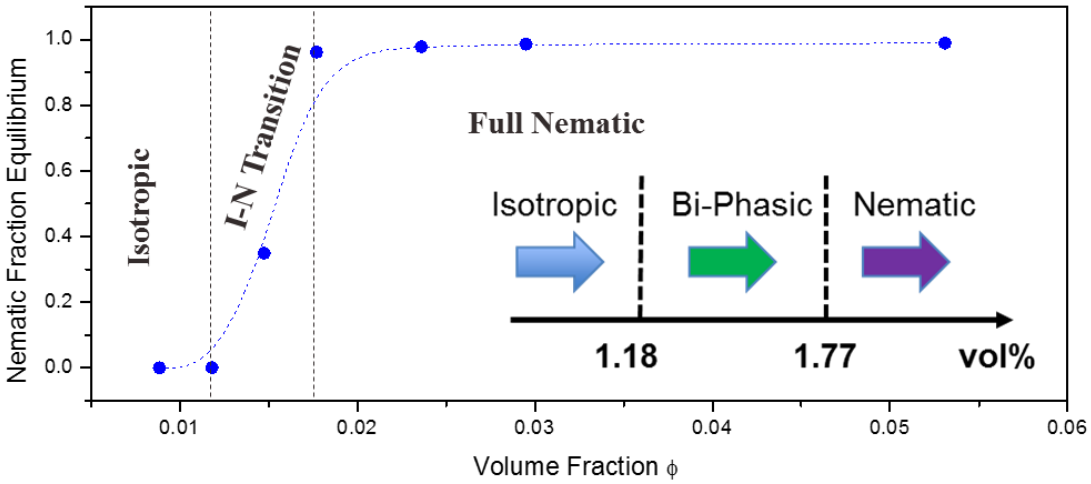

Figure 15. Fraction of nematic phase as a function of volume fraction for small platelets. The phase diagram is divided into three regions: isotropic, I-N, and nematic.

The basic principle of the two different phase diagrams is that for small platelets, the nucleation growth sediments faster than the larger platelets. Also, the I-N transition occurs faster for small platelets. This has already been confirmed experimentally[29]. The reason is that for smaller platelets, they overcome faster diffusion and translation rates; thus, the nuclei of the tactoids grows larger and the terminal velocity of the tactoids is faster. This means that the sedimentation of nematic crystalline will occur faster for small inverse aspect ratios, *i.e.* smaller platelets[50].

CHAPTER III

ELECTRIC BIREFRINGENCE MEASUREMENTS

Birefringence is an optical property of liquid crystals because they have a refractive index that depends on the polarization and propagation of the light. The electric birefringence is also a traditional method to study the field-induced orientation of the platelets[15, 51]. This occurs in nematic, smectic, and crystalline phases. However, liquid crystals are very sensitive to an electric field and can make an isotropic phase, which has no birefringence, exhibit anisotropy. The property of liquid crystals to be responsive to an electric field can allow applications of display and other optical device technology. Since the beginning of the century, there have been extensive studies in electro-optical properties of liquid crystals that led to discoveries such as electrohydrodynamic instability[52], Frederiks transition[53], ferroelectric switching[54], induced biaxiality[55], etc. The optical anisotropy of a liquid crystal is called birefringence, and it is defined by the equation

$$\Delta n = n_e - n_o = n_{\parallel} - n_{\perp}$$

where $n_{\parallel}$ and $n_{\perp}$ are the refractive index components parallel and perpendicular to the director of the disk, respectively. In the isotropic phase, the liquid phase does not exhibit any birefringence because the interactions between neighboring platelets are too weak to induce an spontaneous long-range orientational order[56-57]. In this section, the induced birefringence of two different size platelets in the dilute region are going to be measured and compared to different colloidal systems.

External Electric Field

An external electric field can influence the orientation of the platelets and this can characterize important electro-optical properties of the material. An electric field causes the disk-like molecules to orient along the direction of the electric field[58]. As a result, this alignment of platelets induces birefringence as shown in **Figure 16**. The ZrP nanoplate suspension of volume fraction of $\phi = 0.001$ and average inverse aspect ratio of 901 was loaded into a Kerr cell that contains two copper electrodes located opposite to each other. A monochromatic light source is placed behind the Kerr cell and analyzer. The advantage of using a Kerr cell is that it provides a uniform electric field in the sample. The Kerr cell can also provide a high sensitive measurement of induced birefringence, as well as enabling to study very dilute suspensions. The Kerr cell has also its disadvantages; for example, it degrades the sample very fast when working at low frequencies. The direct contact of the electrolytes to the copper electrodes results in a strong current in the suspension that can cause sample degradation. This degradation is often seen because of the strong polarization created by the electrodes, Faradaic reactions, or electrolysis. However, sample degradation can be avoided. The sample should not be exposed to an AC electric field at low frequencies because it often results of electrolysis.

For this experiment, the induced birefringence of ZrP nanoplates will be measured using image analysis. The copper electrodes are 3 millimeters apart with optical path length of 10 millimeters. The Kerr cell is placed between two cross polarizers, the polarizer is 45° off the vertical axis, and the analyzer is set perpendicular

making an angle of 135° from the vertical axis. As seen in **Figure 16**, the isotropic suspension shows optical birefringence as the electric field increases. The electric field was operated at high frequency, 300 kHz, to avoid electrolysis. At low frequencies, chemical reduction and electrolysis[59] were observed. All experiments were set above 1 kHz to avoid the formation of bubbles. The reason is that in the beginning, when there is not application of electric field, platelets are in random orientation and no long-range orientational order is seen. As the electric field increases, the director of the platelet aligns perpendicular to the field. The presence of an electric field changes the orientation of the platelets through direct induced electric dipole or through indirect viscous forces. Due to both cases, the orientational distribution of particles $f(\theta)$ becomes anisotropy, where θ is the angle between the electric field and the symmetry axis of the particle. The relationship between the macroscopic birefringence, as seen in **Figure 16**, and the orientational distribution of particles $f(\theta)$ is shown as[60]

$$\Delta n = \Delta n_{sat} \phi \langle P_2(cos\theta) \rangle$$

where θ is the volume fraction of the platelets, $\langle P_2(cos\theta) \rangle$ is the average of the second Legendre polynomial which quantifies the degree of alignment of particles, and

$$\Delta n_{sat} = \frac{\Delta \alpha^0}{2 n_s \varepsilon_0 V_P}$$

where $\Delta \alpha^0$ is the optical polarizability, n_s is the refractive index of the solvent, ε_0 is the vacuum permeability, V_P is the volume of the particle. This is called the specific birefringence when there is perfect aligned system and volume fraction of $\phi = 1$.

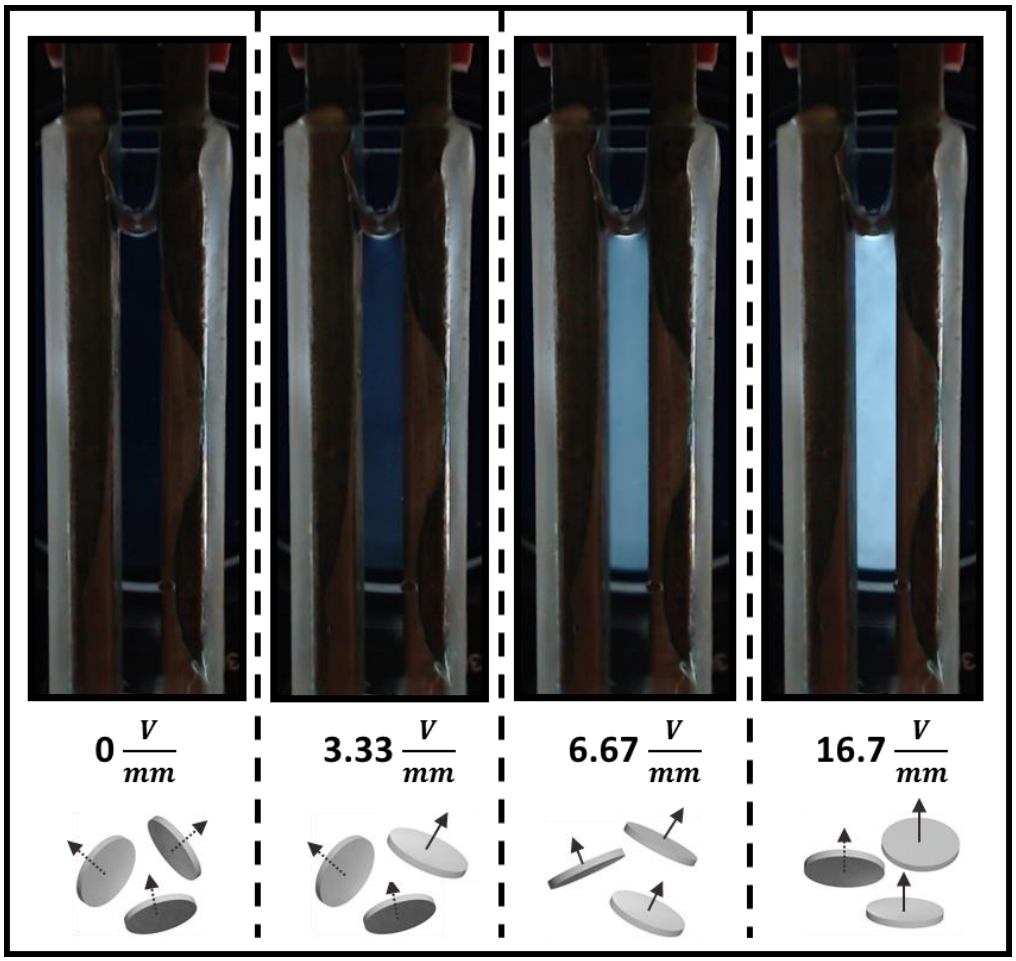

Figure 16. Electric field effect in isotropic suspensions of nanoplates. As the electric field is increased, the director of the platelet is forced to align perpendicular to the electric field due to electric and hydrodynamic torques; thus, inducing a well-ordered system that shows birefringence. The Kerr cell is between two cross polarizers and front of a monochromatic light source. This was done at constant frequency of 300 kHz.

The induced birefringence for this system can be obtained by doing image analysis tools. A code was created to estimate the intensity of the birefringence as a function of electric field. The sample becomes lighter as the electric field increases; hence, the code can estimate the value of the intensity, defined as ‘average grayscale’.

Once the grayscale values were obtained, it can then be converted into transmittance as shown in the following equation[50]

$$\text{Trasmittance} = \frac{I}{I_0} = \left(\frac{avg.\ grayscale}{256}\right)^{2.4}$$

The average effective birefringence $\langle \Delta n_{eff} \rangle$ is defined as[61]

$$\Delta n_{eff} = sin^{-1}\left(\sqrt{\frac{I}{I_0}}\right)\left(\frac{\lambda}{\pi l}\right)$$

where I/I_0 is the transmittance value, λ is the wavelength of the incident light, and *l* is the optical path length.

Since the values of transmittance are already known, then the average effective birefringence can be estimated. This is shown in **Figure 17**. From the plot, the value of the saturation birefringence is the plateau of the signal, when the platelets have achieved perfect orientation. It is in the order of 10^{-5}, but again, this is only an estimation because it was done with image analysis tools. A more accurate method to measure induced birefringence will be explained later.

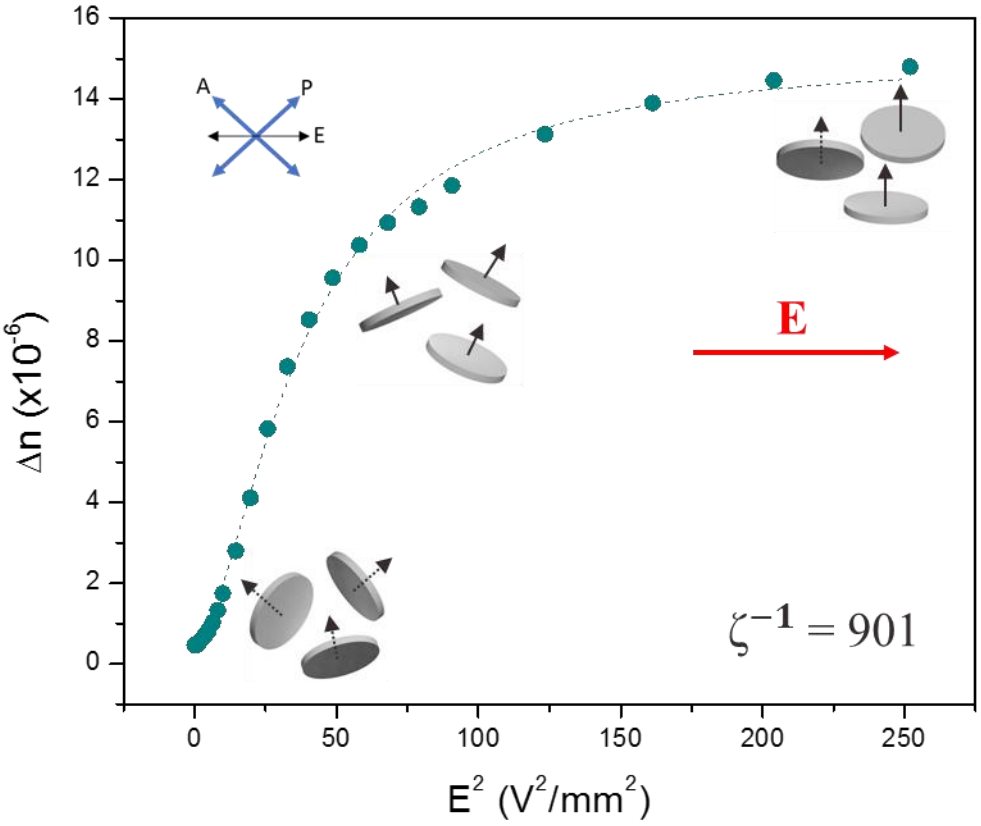

Figure 17. Electric field induced birefringence in isotropic suspension of ZrP platelets ($\phi = 1.00x10^{-3}$). The Kerr cell is between crossed polarizers 45° to the electric field direction. Measurement of induced-birefringence as a function of electric field squared using image analysis. Perfect alignment of platelets is achieved when the electric field is high enough.

Electro-Optical System Derivation

Electro-optical devices can detect changes in their optical properties in the medium, such as birefringence. The Kerr cell is used to determine the birefringence which is proportional to the square of the electric field. However, electro-optical systems can be described by using Jones matrix calculus for polarized light discovered by J.C. Jones[62-64]. This derivation[65] will allow to correct the measurements of the electric birefringence, also known as the Kerr effect, of very diluted suspensions where the stress-induced birefringence of the Kerr cell wall cannot be neglected. This correction method includes rotating polarizers (polarizer and analyzer) and a quarter wave plate. The use of the quarter wave plate has several advantages: the sign of the birefringence can be obtained with this procedure; the precision of the measurement is larger; the influence of the stress-induced birefringence of the windows of the Kerr cell is minimized.

The following procedure to make birefringence measurements is derived from Jones matrixes[65]. Retarder is characterized by optical retardation, δ, using the unitary matrix

$$\mathbf{J}(\delta,\theta) = \begin{bmatrix} e^{\frac{i\beta}{2}}cos^2(\theta) + e^{-\frac{i\beta}{2}}sin^2(\theta) & \left(e^{\frac{i\beta}{2}} - e^{\frac{i\beta}{2}}\right)\sin(\theta)\cos(\theta) \\ \left(e^{\frac{i\beta}{2}} - e^{\frac{i\beta}{2}}\right)\sin(\theta)\cos(\theta) & e^{\frac{i\beta}{2}}sin^2(\theta) + e^{-\frac{i\beta}{2}}cos^2(\theta) \end{bmatrix}$$

where θ is the angle between the x-axis and the fast axis.

Also, both the rotator, **R**, and polarizer, **P**, can be described using unitary matrix as

$$\boldsymbol{R}(\theta) = \begin{bmatrix} cos(\theta) & sin(\theta) \\ -sin(\theta) & cos(\theta) \end{bmatrix} \text{ and}$$

$$\boldsymbol{P}(\theta) = \begin{bmatrix} cos^2(\theta) & sin(\theta)\,cos(\theta) \\ sin(\theta)\,cos(\theta) & sin^2(\theta) \end{bmatrix}.$$

The following derivation involves properties of a combination of different retarders. The unitary matrix can be expressed in terms of Pauli matrixes,

$$\boldsymbol{i} = \begin{bmatrix} i & 0 \\ 0 & -i \end{bmatrix}, \boldsymbol{j} = \begin{bmatrix} 0 & 1 \\ -1 & 0 \end{bmatrix}, \boldsymbol{k} = \begin{bmatrix} 0 & i \\ i & 0 \end{bmatrix}$$

where $\mathbf{i^2} = \mathbf{j^2} = \mathbf{k^2}, \mathbf{i} \cdot \mathbf{j} = \mathbf{k}, \mathbf{i} \cdot \mathbf{k} = \mathbf{j}, \mathbf{j} \cdot \mathbf{k} = \mathbf{i}$.

Then the rotator and retarder can be simplified as

$$\boldsymbol{R}(\theta) = cos(\theta)\boldsymbol{I} - sin(\theta)\boldsymbol{j} \text{ and}$$

$$\boldsymbol{J}(\delta, \theta) = cos\left(\delta/_2\right)\boldsymbol{I} + sin\left(\delta/_2\right)cos(2\theta)\,\boldsymbol{i} + sin\left(\delta/_2\right)sin(2\theta),$$

respectively. When a quarter wave plate is placed in the system with fast-axis parallel to the incident polarization, then the output vector can be described as

$$\boldsymbol{v} = \boldsymbol{P}\left(\pi/_2 - \alpha\right)\boldsymbol{J'}\left(\pi/_2, 0\right)\boldsymbol{J}(\delta, \pi/_4)\boldsymbol{v}_0.$$

Using Pauli matrixes, the quarter-wave plate, **J'**, and retarder, **J**, can be found as

$$\boldsymbol{J'} = 2^{-\frac{1}{2}}(\boldsymbol{I} + \boldsymbol{i}) \text{ and}$$

$$\boldsymbol{J} = cos\left(\delta/_2\right)\boldsymbol{I} + sin\left(\delta/_2\right)\boldsymbol{k},$$

respectively. Then by applying the equivalence theorem, the transmitted intensity of the beam is found as

$$I = I_i sin^2(\alpha + \frac{\delta}{2})$$

where I_i is the intensity of the incident beam, $(\pi/2 - \alpha)$ is the angle between the analyzer and incident polarization, and δ is the phase different of the extraordinary and ordinary rays of the light.

This phase difference[66] is expressed as

$$\delta = \frac{2\pi d \Delta n}{\lambda}$$

where Δn is the induced birefringence expressed as the difference between extraordinary refractive index and ordinary refractive index.

The intensity of the transmitted intensity when the Kerr cell does nothing, having polarizer, analyzer, and quarter-wave plate, is shown as

$$I_0 = I_i sin^2 \alpha.$$

Solving both equations of I_0 and I simultaneously in terms of the intensity of the light beam, then the induced-birefringence equation is expressed as

$$\Delta n = \frac{\lambda}{\pi d}\left(arcsin\left(\sqrt{\frac{I}{I_0}} sin\alpha\right) - \alpha\right).$$

Electric Birefringence Spectroscopy

Electric birefringence spectroscopy (EBS) is a powerful tool that can provide enough information on the interfacial properties of colloidal suspensions[67]. It can also provide information on the different polarization mechanics of the platelets, as well as relevant information on their electric double layers[14]. Using EBS, it can measure the induced birefringence of the system accurately through an application of an AC electric field. This innovated technique can provide valuable information on the electro-kinetic phenomena, as well information on the electric and optical properties of the particle such as surface conductivity and refractive index[14, 68]. Despite the potential use of EBS, only few studies are devoted to this technique[17]. This technique provides quantitative analysis of the high frequency spectra of the system. For these reasons, EBS will be used to measure the anisotropy of polarizability of ZrP platelets.

Before measuring the spectrum, there are some key points that should be taken into consideration.

1. The ionic strength of the sample. The particle orientation is determined by the structure of the charge at the interface, which is related to the ionic strength.
2. Monitor the electric field for every measurement. This will allow to check the intensity and shape of the signal that it is applied to the sample.
3. The Kerr law must be satisfied for different frequencies, and the range of the amplitude of the electric field should lie in the Kerr regime. The saturation of the signal can be related to the power that the amplifier can provide. If the ionic

strength of the sample is very high, then the resistance is very low and the power needed to get large voltage is high.

4. The dilution of the suspension. Different volume fractions should be measured to confirm that the Kerr coefficient is proportional to the particle concentration; this will confirm if the sample is in the dilute regime. Another way to determine this is to establish a phase diagram for the system.
5. The transient behavior. Once the signal is off, the decay time of the Kerr coefficient can be used to calculate the size of the particles. Another way to determine the size of the particles is to perform dynamic light scattering measurements.
6. If all points are well-addressed, then the spectrum could result of the Maxwell-Wagner-O'Konski relaxation[68]. The orientation of the particle is due to the induced dipole. This induced dipole should decrease near-around the MHz range, which depends on the conductivity, because particle charge and ionic strength does not play a major role in this region[14].

The Electric Birefringence Spectroscopy (EBS) set-up is shown in **Figure 18**, and it includes: He-Ne laser beam (Thorlabs, HNLS008L, λ = 633 nm), polarizer (Thorlabs), quarter-wave plate (Thorlabs, λ/4 at 633 nm), analyzer (Thorlabs), photodetector (DET36A, Thorlabs), an oscilloscope (Tektronix, TBS 1052B), a voltage generator (Stanford Research Systems, Model DS345), an amplifier (Falco Systems, WMA-100), and a hand-made quartz Kerr cell. Details about the experiment is described in the book, *Electric Dichroism and Electric Birefringence*[67].

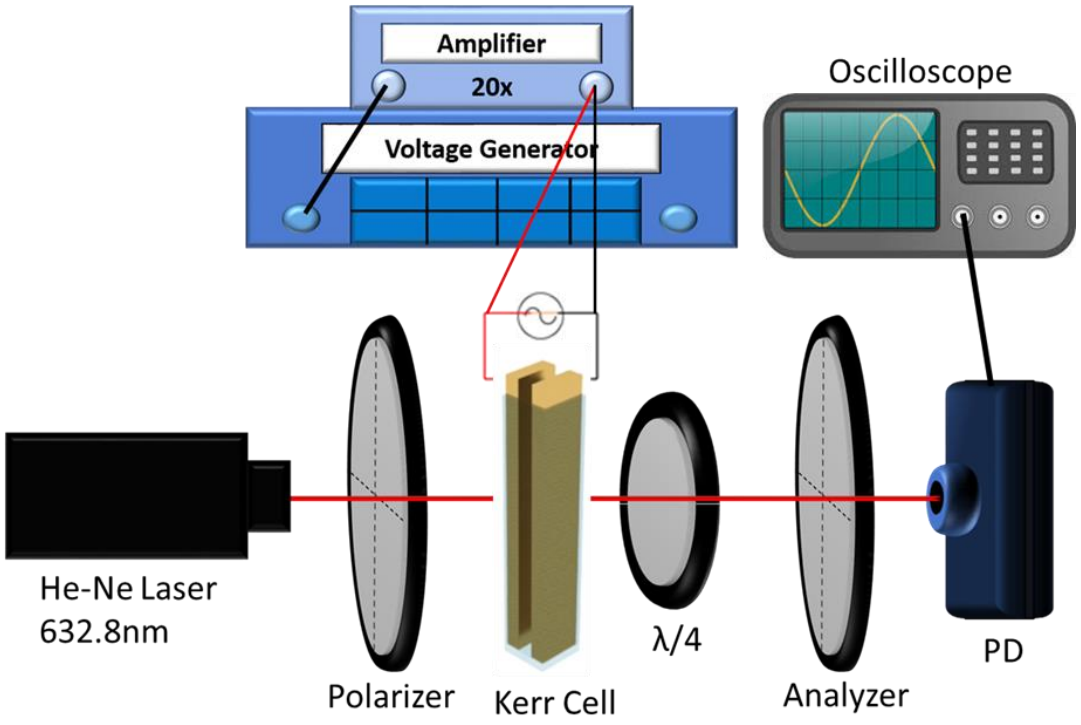

Figure 18. Electric Birefringence Spectroscopy (EBS) set-up to measure the electro-optic properties of colloidal suspensions.

A linearly polarized He-Ne laser beam (λ = 633 nm) transverses through:

i. A polarizer rotated at 45° to the direction of the electric field.

ii. A Kerr cell containing the suspension. The optical path length of the cell is 1 mm, and the copper electrodes are 2 mm apart. The copper electrodes will create an electric field that is perpendicular to the laser beam and 45° to the incident polarization.

iii. A quarter wave plate whose fast axis is parallel to the incident polarization. The quarter wave plate is used to minimize the residual birefringence of the cell window.

iv. An analyzer that is (90° - α) to the incident polarization. The analyzer is rotated in a way that the angle α maximizes the signal of the transmitted intensity and it will also compensate the birefringence losses caused by the cell wall.

v. A photodiode. The transmitted intensity is collected by the photodetector and then sent to an oscilloscope for data analysis.

The data collected from the oscilloscope will give the intensity as a function of time. Then Δn is extracted by using the following expression[17, 65]

$$\Delta n = \frac{\lambda}{\pi d}\left(arcsin\left(\sqrt{\frac{I}{I_0}}sin\alpha\right) - \alpha\right).$$

where I_0 is the intensity when there is no electric field.

Small-Angle X-Ray Scattering (SAXS)

Patrick Davidson from the Laboratoire de Physique des Solides, along with Ivan Dozov, made collaboration with us. He measured the induced birefringence of our zirconium phosphate platelet in a capillary with aluminum electrodes of 2 mm apart and provided us with the SAXS measurement. He found out that the platelets have perfect orientational order of S = -0.5 when a high electric field is applied. This measurement will be very useful when finding the anisotropy of polarizability ($\Delta\alpha$). This means that a strong anisotropy was induced by the electric field and that the platelets align with their plane parallel to the field as shown in **Figure 19**. This effect is called, 'anti-nematic'[57].

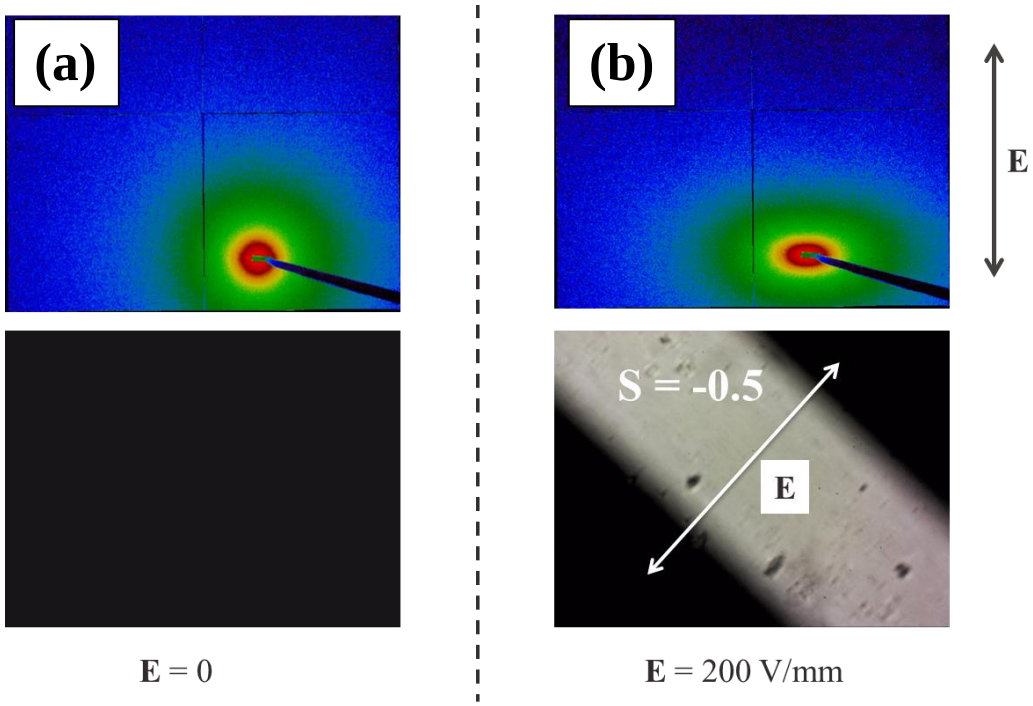

Figure 19. SAXS patterns of the isotropic phase of zirconium phosphate platelets of ϕ = 0.041%. (a) Without electric field. (b) With electric field (400 V, l = 2 mm, ν = 600 kHz)

Induced Birefringence Measurements

Before the electric birefringence measurements, the two mother suspensions of inverse aspect ratio of 901 and 290 were diluted into the same concentration: $\phi = 0.001$, $\phi = 0.002$, and $\phi = 0.003$. It is very convenient to have them in the same concentration to be able to compare them. However, the biphasic region of each platelet is different due to their size distribution. The biphasic region of large platelets lie between $4.62x10^{-3} < \phi < 1.98x10^{-2}$ and the biphasic region of small platelets lie between $1.18x10^{-2} < \phi < 1.77x10^{-2}$. The induced birefringence was measured using the Electric Birefringence Spectroscopy (EBS) as it was explained in the previous section. The induced birefringence Δn as a function of the electric field squared are shown in **Figure 20** to **Figure 27** for different volume fractions ϕ for zirconium phosphate platelets. All the samples were diluted below the biphasic region because measurements of electric birefringence only apply to isotropic samples. Also, all the measurements were taken at 300 kHz with increasing electric fields. For all volume fractions, there is an initial quadratic increase for electric fields which is the Kerr region[69]. Depending on the size of the platelet, volume fraction, and ionic strength, this Kerr regime is different. One observation that was seen is that the addition of salt decreases the induced birefringence. The birefringence decreases because salt gives rise to an increase in electrolyte conductivity which enhances interflake interaction. Also, the rotational relaxation of the particles slowed down with the addition of TBACl.

Figure 20 shows the induced birefringence as a function of electric field squared for large platelets. At different volume fractions, the slope at low electric fields, the Kerr regime, gets sharper at increasing concentration. At higher fields, the birefringence saturates to a ϕ-plateau, and this is when the colloidal particles are perfectly aligned.

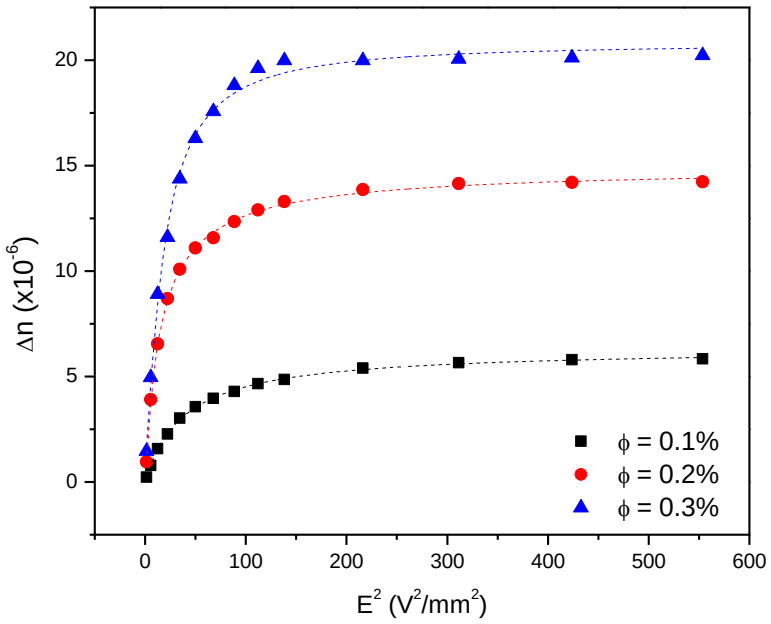

Figure 20. Induced birefringence for large platelets of inverse aspect ratio 901 as a function of E^2. Measurements for three different volume fractions in the dilute region.

For very low volume fractions, all the particles are independent to each other. The induced birefringence can be approximated as[70]

$$\Delta n = \Delta n^P \phi S(E)$$

where Δn^P is the specific birefringence of the particles, *i.e.*, when the birefringence is extrapolated to ϕ = 1 and the system is perfectly ordered. The induced orientational order parameter *S* (E) is given by[57]

$$S(E) = \frac{1}{2} < 3cos^2\theta - 1 >$$

$$= \frac{1}{2}\int_0^1 f(\theta)(3cos^2\theta - 1)dcos\theta$$

where $f(\theta)$ is the orientational function of particles.

The induced birefringence equation is only valid at very diluted suspensions because the average optical susceptibility cannot longer improve. As the system gets closer to the biphasic region, the saturation values of birefringence cannot longer increase. This is due to the interference of the optical fields with particles who are very close to each other.

From SAXS experiments, it was measured that at high electric fields, the zirconium phosphate platelets have an induced orientational parameter of $S(E) = -0.5$. This value will now be used to estimate the specific birefringence.

The saturated birefringence value is linearly proportional to the concentration as seen in **Figure 21**. The saturation values were obtained from an extrapolation of the measured birefringence as the electric field squared approaches to infinity ($E^2 \rightarrow \infty$). The local volume fraction of about $\phi \approx 0.003$ was obtained from the phase diagram. This local volume fraction is the equilibrium value for the isotropic phase in coexistence with the nematic phase[57]. The specific birefringence can be obtained by fitting a linear equation to the saturation values and dividing the slope with the order parameter.

The specific birefringence for the large platelets of aspect ratio 901 was found to be $\Delta n^P = -0.0158 \pm 0.0015$. This value will later be used to calculate the anisotropy polarizability for zirconium phosphate platelets.

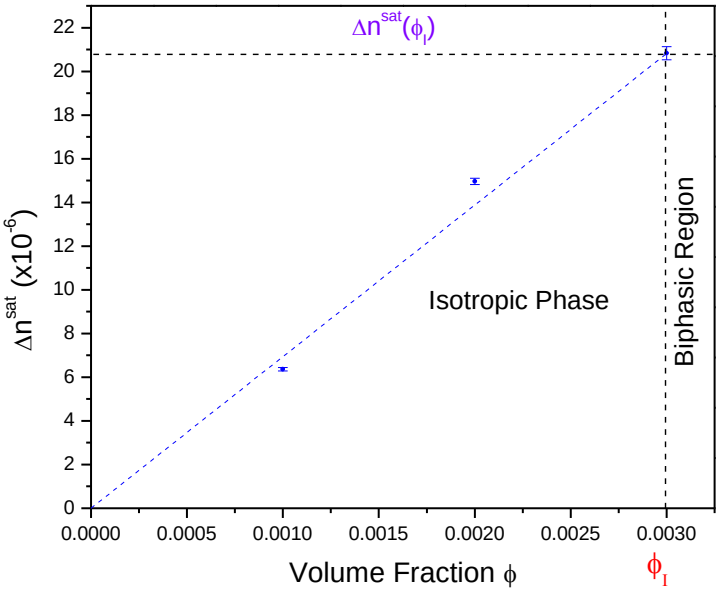

Figure 21. Measurements of saturated birefringence $\Delta\mathbf{n}^{\boldsymbol{sat}}(\boldsymbol{\phi})$ under the isotropic region for large platelets of inverse aspect ratio 901.

The addition of salt caused a decrease in birefringence as shown in **Figure 22**; thus, it decreased the sensitivity of the electro-optic response to electric fields. The saturation values of birefringence decreased with a factor of 2 as shown in **Figure 23**. The reason is that an increase in ionic strength, it induces a decrease in the electric double layer thickness which brings a decrease in the electric potential. Adding 1 mM of TBACl to the suspension, the specific birefringence of the large platelet decreases to $\Delta n^P = -0.007038 \pm 0.000081$.

The same measurements were done for small platelets. As the particle gets smaller, the induced birefringence decreases. Therefore, the induced birefringence is a function of ionic strength, aspect ratio, and volume fraction. This is in good agreement with the following expression[71],

$$\Delta n = \phi(n_P - n_S)\frac{9k}{(9+k)^2}\left(L_{\parallel} - L_{\perp}\right)S$$

where S (E) is the field-induced order parameter defined as $S(E) = \Delta n(E)/\Delta n^{sat}(\phi)$, k is written as $(1-\phi)/(n_P^2/n_S^2 - 1)$, $L_{\parallel}$ and $L_{\perp}$ are the depolarizing factors depending on particle symmetry and are defined as $L_{\parallel} \approx 1 - {}^{\pi a}/_{2b}$ and $L_{\perp} \approx {}^{\pi a}/_{4b}$. This function is only a function of aspect ratio and volume fraction, but another equation that involves the effect of ionic strength will be explained later. The specific birefringence for the small platelets of aspect ratio 290 changed to $\Delta n^P = -0.00216 \pm 0.000083$. An addition of 1 mM of TBACl decreased this value to $\Delta n^P = -0.001528 \pm 0.000146$.

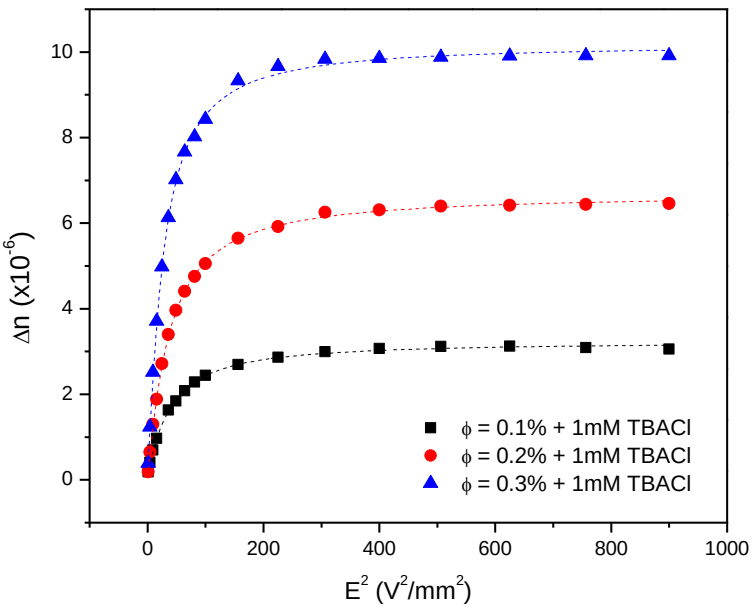

Figure 22. Induced birefringence for large platelets of inverse aspect ratio 901 as a function of E^2. Measurements for three different volume fractions in the dilute region with the addition of 1 mM TBACl.

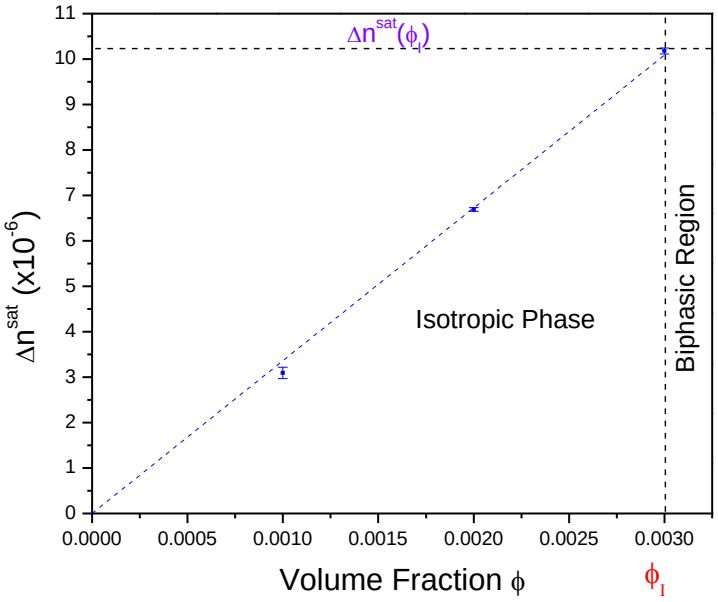

Figure 23. Measurements of saturated birefringence $\Delta \mathbf{n}^{\boldsymbol{sat}}(\boldsymbol{\phi})$ under the isotropic region for large platelets of inverse aspect ratio 901 with the addition of 1 mM TBACl.

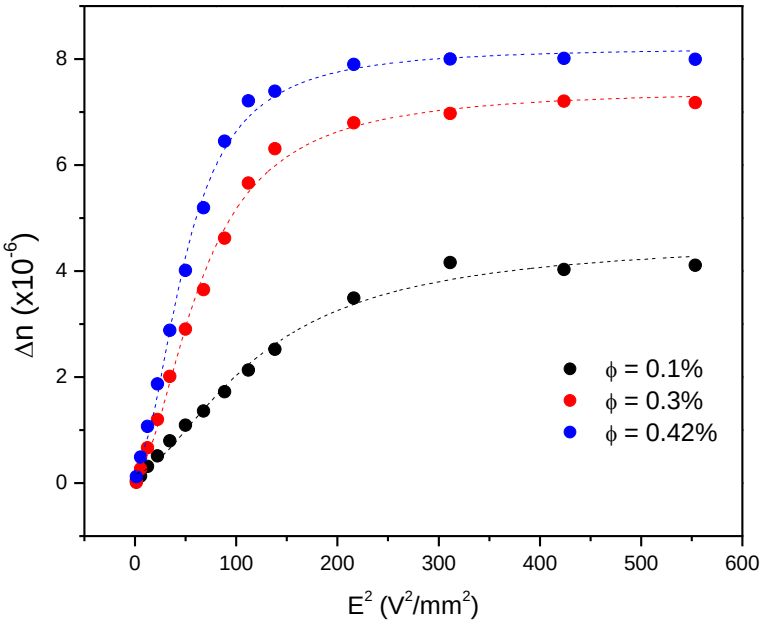

Figure 24. Induced birefringence for small platelets of inverse aspect ratio 290 as a function of E^2. Measurements for three different volume fractions in the dilute region.

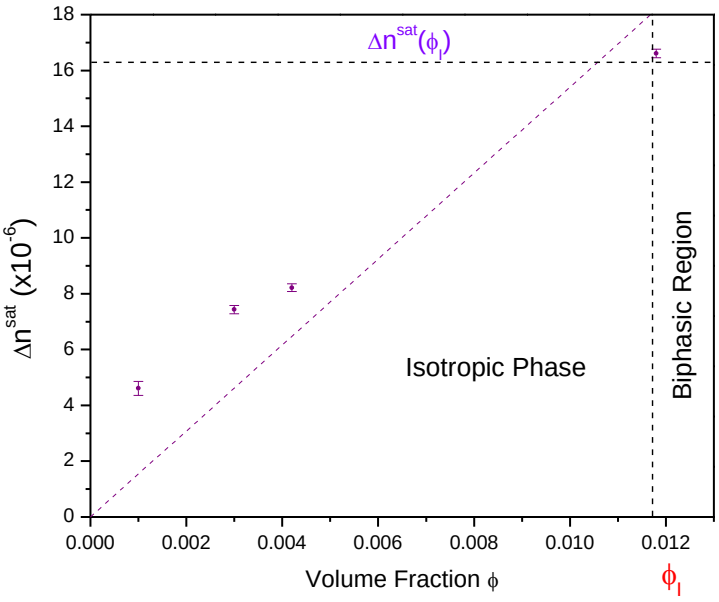

Figure 25. Measurements of saturated birefringence $\Delta \mathbf{n}^{sat}(\boldsymbol{\phi})$ under the isotropic region for small platelets of inverse aspect ratio 290.

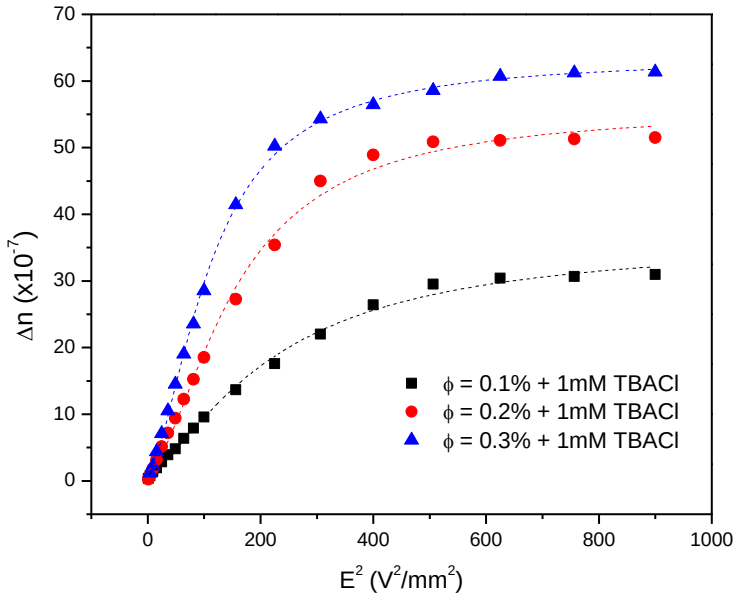

Figure 26. Induced birefringence for small platelets of inverse aspect ratio 290 as a function of E^2. Measurements for three different volume fractions in the dilute region with the addition of 1 mM TBACl.

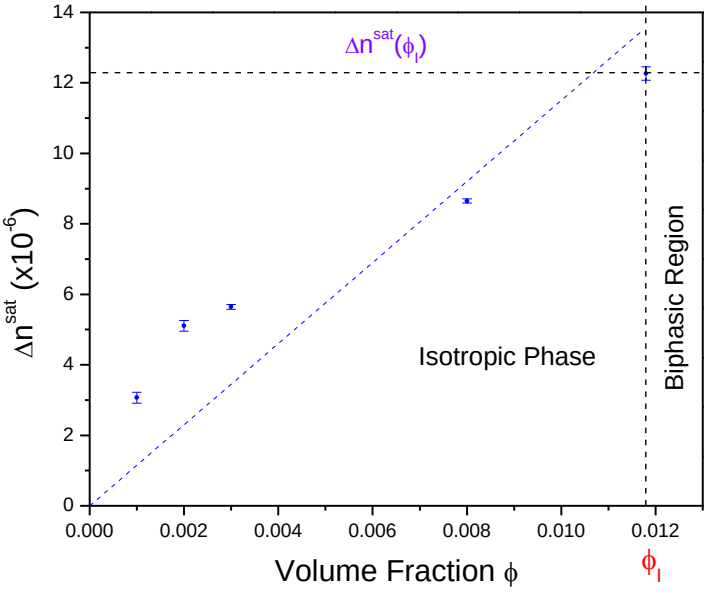

Figure 27. Measurements of saturated birefringence $\Delta\mathbf{n}^{\boldsymbol{sat}}(\boldsymbol{\phi})$ under the isotropic region for small platelets of inverse aspect ratio 290 with the addition of 1 mM TBACl.

The induced birefringence and the effective electric field are related to the Kerr effect. As the voltage keeps increasing, the orientation of the nanoplates gets driven by the field. The Kerr constant is defined as[72]

$$\Delta n(E) = C_K(\phi)E^2$$

where C_K is the Kerr coefficient[73-75]. This equation is only valid in the low regions and the effect diverges as E → ∞. From **Figure 20** to **Figure 27**, the Kerr coefficient can be calculated and values are shown on **Table 1** to **Table 4**.

ZrP Nanoplates $\zeta^{-1} = 901$	
Volume Fraction (%)	**Kerr Constant (mm^2/V^2)**
0.1	0.1213×10^{-6}
0.2	0.4925×10^{-6}
0.3	0.8405×10^{-6}

Table 1. Kerr coefficient as a function of volume fraction, ϕ, for large platelets.

ZrP Nanoplates $\zeta^{-1} = 901$ + 1 mM TBACl	
Volume Fraction (%)	**Kerr Constant (mm^2/V^2)**
0.1	0.5135×10^{-7}
0.2	1.1192×10^{-7}
0.3	1.6184×10^{-7}

Table 2. Kerr coefficient as a function of volume fraction, ϕ, for large platelets with the addition of salt.

ZrP Nanoplates $\zeta^{-1} = 290$	
Volume Fraction (%)	**Kerr Constant (mm^2/V^2)**
0.1	1.6359×10^{-8}
0.2	3.8759×10^{-8}
0.3	5.9834×10^{-8}

Table 3. Kerr coefficient as a function of volume fraction, ϕ, for small platelets.

ZrP Nanoplates $\zeta^{-1} = 290$ + 1 mM TBACl	
Volume Fraction (%)	**Kerr Constant (mm^2/V^2)**
0.1	0.7888×10^{-8}
0.2	1.7660×10^{-8}
0.3	2.7291×10^{-8}

Table 4. Kerr coefficient as a function of volume fraction, ϕ, for small platelets with the addition of salt.

Since the Kerr constant is a function of birefringence, a change in size, volume fraction, or ionic strength, will make a difference to the Kerr coefficient. This was proven in the tables and are in good agreement with the expression of Kerr constant and induced birefringence.

CHAPTER IV

MAXWELL-WAGNER-O'KONSKI

An electrokinetic model should be able to provide insightful information on the polarizability of a spheroid particle in terms of size, charge of the particle, and ionic strength of the solution. This polarizability arises from the mismatch of conductivities between the solvent and the particle. The ionic mobility in the electrical double layer has also an effect in the polarizability of the particle. The electric polarization of the particle can be determined from the dielectric body of the material suspended in a dielectric medium, such as the electrolyte solution. This classical problem was first solved by Maxwell[76]. Later in the years, Wagner decided to extend this application to spheres[77]. And finally, this technique was extended by O'Konski to charged particles with effective surface conductivities. This contribution led to the formation of a new regime often referred as Maxwell-Wagner-O'Konski (MWO) model. The goal is to see if the electric polarizability of zirconium phosphate platelets can be expressed based on the MWO regime.

Theory of Anisotropy of Polarizability

Colloidal systems exhibit an induced dipole moment when they are influenced by an external field. The induced dipole moment is governed by[78]

$$\vec{p} = \alpha_0 \overrightarrow{E(t)}$$

where α_0 is the anisotropy tensor of the particle employed at low frequencies.

The Maxwell-Wagner-O'Konski polarizability of platelets can be expressed as follows[14, 68, 79-80]

$$\alpha_{\|,\perp}^{e} = \frac{4\pi ab^2}{3}\varepsilon_0\varepsilon_s\frac{K_p^* - K_s^*}{K_s^* + (K_p^* - K_s^*)L_{\|,\perp}}$$

where K_p^* and K_s^* are the complex conductivities of the particle and medium, respectively, $2a$ is the thickness of the material, and $2b$ is the diameter of the system.

Real part of polarizability can be expressed as function of $\alpha_{\|,\perp}^{\infty}$ and $\alpha_{\|,\perp}^{0}$

$$\alpha_{\|,\perp} = \alpha_{\|,\perp}^{\infty} + \frac{\alpha_{\|,\perp}^{0} - \alpha_{\|,\perp}^{\infty}}{1 + \omega^2\tau_{\|,\perp}^2}$$

where $\alpha_{\|,\perp}^{\infty}$ and $\alpha_{\|,\perp}^{0}$ are the MW polarizabilities at high and low frequencies, respectively, and $\omega = 2\pi f$ is the ionic relaxation frequency.

In this case, $\tau_{\|,\perp}$ are the reciprocals of MW cut-off frequencies, and they are defined as followed:

$$\tau_{\|,\perp} = \varepsilon_0\frac{(1 - L_{\|,\perp})\varepsilon_s + L_{\|,\perp}\varepsilon_p}{(1 - L_{\|,\perp})K_s + L_{\|,\perp}K_{p,\|,\perp}}$$

$\alpha_{\|,\perp}^{\infty}$ and $\alpha_{\|,\perp}^{0}$ are defined as followed:

$$\alpha_{\|,\perp}^{\infty} = \frac{4\pi ab^2}{3}\varepsilon_0\varepsilon_s\frac{\varepsilon_p - \varepsilon_s}{\varepsilon_s + (\varepsilon_p - \varepsilon_s)L_{\|,\perp}}$$

$$\alpha_{\|,\perp}^{0} = \frac{4\pi ab^2}{3}\varepsilon_0\varepsilon_s\frac{K_{p,\|,\perp} - K_s}{K_s + (K_{p,\|,\perp} - K_s)L_{\|,\perp}}$$

As stated by the O'Konski's model[81], a strong effective particle conductivity is produced by the electrical double layer which depends on the geometrical factor of the platelets.[57]

$$K_{p,\perp} = \frac{K_{\perp}^{S}}{a} \qquad\qquad K_{p,\parallel} = \frac{2K^{S}}{b}$$

where K^S is the surface conductivity and can be estimated as $\mu_s q$.

By the Gouy-Chapman equation[82-83], the surface charge density is expressed as

$$q = \frac{2\varepsilon\kappa k_B T}{ze}\sinh\left(\frac{ze\zeta}{2k_B T}\right)$$

where ε is the dielectric constant, e = 1.6x10^{-19} Coulombs, z is the valency of the counterions, and the Debye length is given by[72]

$$\kappa^{-1} = \sqrt{\frac{k_B T \varepsilon_0 \varepsilon_s}{2e^2 N_A I}}$$

where I is the ionic strength of the substance.

The depolarized factor of infinitely thin nanoplates can also be estimated as

$$L_{\parallel} \approx 1 - \frac{\pi a}{2b} \qquad\qquad L_{\perp} \approx \frac{\pi a}{4b}$$

The theoretical anisotropy of polarizability can be obtained by

$$\boxed{\Delta\alpha = \alpha_{\parallel} - \alpha_{\perp}}$$

Maxwell-Wagner-O'Konski Model

According to the model, the anisotropy of polarizability (Δα) depends on aspect ratio, volume, and ionic strength on its surface. For this reason, Δα will be calculated experimentally for different aspect ratios, different volume fractions, and different surface conductivities. The two different aspect ratios that will be tested are 901 and 290. Three different concentrations, in the dilute region, will be used for this study as 0.001, 0.002, and 0.003. The calculated surface conductivities for both platelets at diluted region are shown in **Table 5** and **Table 6**.

ZrP Nanoplates	
Aspect Ratio ζ^{-1}	**Surface Conductivity (S)**
901	1.22949×10^{-10}
290	8.95837×10^{-10}

Table 5. Measurements of surface conductivities at different aspect ratios when no salt is added.

ZrP Nanoplates + 1 mM TBACl	
Aspect Ratio ζ^{-1}	**Surface Conductivity (S)**
901	7.27792×10^{-11}
290	1.1654×10^{-10}

Table 6. Measurements of surface conductivities at different aspect ratios when 1 mM of TBACl is added.

To measure Δα experimentally using the obtained electro-optical measurements from the EBS, an expression should be obtained[84]. The relationship between the induced birefringence and Kerr coefficient is defined by the following expression

$$\Delta n = K\lambda E^2$$

In colloidal suspension, the induced birefringence can be expressed as

$$\Delta n = \Delta n^P \phi S(E)$$

where Δn^P is constant and the specific birefringence, volume fraction ϕ can be rewritten as $\frac{\phi}{1-\phi/\phi^*}$, ϕ^* is the spinodal volume fraction which will be explained later, *S* (E) is the nematic order parameter.

The nematic order parameter, when there are no interparticle interactions, can be defined as

$$S(E) = \int_0^\pi \left(\frac{3}{2}cos^2\theta - \frac{1}{2}\right) f(\theta, E) sin\theta d\theta$$

where $f(\theta, E)$ is the Boltzmann distribution and it has a potential of

$$U(\theta) = \frac{1}{2}\Delta\alpha E^2 cos^2\theta$$

The Boltzmann distribution can be expressed as

$$f(\theta, E) = \frac{e^{-\frac{U(\theta)}{k_B T}}}{\int_0^\pi e^{-\frac{U(\theta)}{k_B T}} sin\theta d\theta}$$

Combining all the equations together, the nematic order parameter then becomes

$$S(E) = \int_0^\pi \left(\frac{3}{2}cos^2\theta - \frac{1}{2}\right) \exp(-Dcos^2\theta)\, sin\theta d\theta \Big/ \int_0^\pi \exp(-Dcos^2\theta)\, sin\theta d\theta$$

where

$$D = \frac{\Delta\alpha}{2k_B T} E^2$$

Since the anisotropy of polarizability involves small amount of electric field, this expression can be reduced to

$$S(E) = \int_0^{\pi} \left(\frac{3}{2} cos^2\theta - \frac{1}{2}\right)(1 - Acos^2\theta) sin\theta d\theta / 2$$

Solving the integral, the nematic order parameter then becomes

$$S(E) = -\frac{\Delta\alpha}{15k_B T} E^2$$

Solving for Δα

$$\Delta\alpha = -\frac{\Delta n}{E^2} \frac{15k_B T}{\Delta n^P} \left(\frac{1 - \phi/\phi^*}{\phi}\right)$$

This expression is only valid when there is no interparticle interaction. To measure the anisotropy of polarizability, Kerr constant ($\Delta n/E^2$), Δn^P, ϕ, and ϕ^* should be measured. From the EBS method, the Kerr constant and specific birefringence were measured for each platelet at different volume fractions as mentioned before. The spinodal volume fraction, ϕ^*, can also be measured from the induced birefringence

measurements from **Figure 28** and **Figure 29**. This technique will be explained in more details.

In **Figure 28**, the electric field induced birefringence is shown as a function of volume fraction, ϕ, for small platelets with the addition of 1 mM of TBACl. The induced birefringence, or Kerr constant, reaches an asymptotic value as it gets closer to the spinodal volume fraction, ϕ^*, and diverges to infinity. The spinodal volume fraction is when the isotropy phase is no longer thermodynamically stable. In other words, it can be said that the volume fraction has left the biphasic region and jumps into the nematic phase at coexistence.

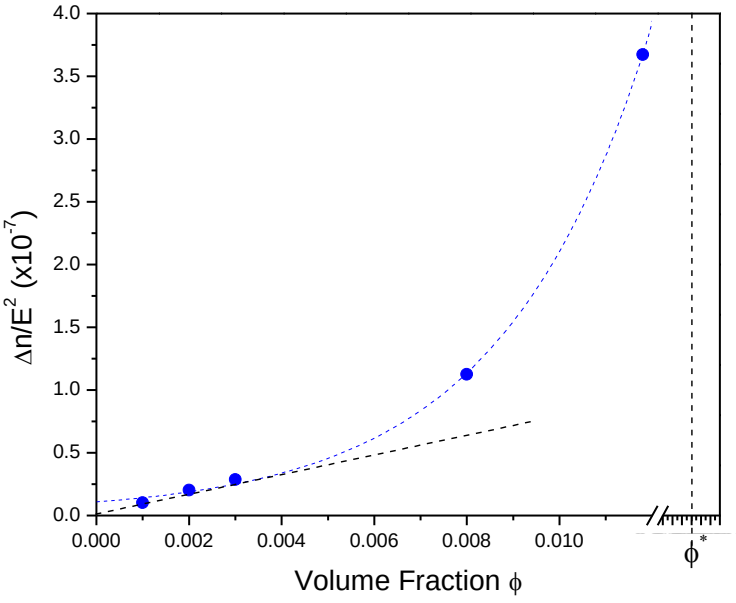

Figure 28. The induced birefringence $\Delta n/E^2$ versus the volume fraction for the small platelet of inverse aspect ratio 290 with the addition of 1 mM TBACl. The induce birefringence diverges as it approaches to the spinodal volume fraction and the vertical asymptote is indicated in dashed lines. As $\phi \rightarrow 0$, the tangent line in the fit curve indicates ideal behavior.

There are many models that explains this critical concentration[85-86] as

$$\phi^* = 16/\pi L^2 D_{eff}$$

where L can be assumed as the thickness of the material and D_{eff} is the effective diameter of the platelet. The effective diameter is expressed as

$$D_{eff} = D(1 + \delta)$$

The effect of the electrostatic interaction on the free energy in the isotropic phase can be interpreted as an increase in the diameter of the disks, and this factor is represented as

$$\delta = \frac{\ln A' + \gamma + \ln 2 - 1/2}{\kappa D}$$

where γ denotes the Euler's constant as 0.5772, $A' = Ae^{-\kappa D}$, A is a proportionality constant[87] defined as $A = 2\pi v_{eff}^2 Q\kappa^{-1}$, the Bjerrum length defined as $Q = e^2/\epsilon k_B T$, ϵ is the permittivity of the solvent, and κ is the Debye length.

In this case, this spinodal volume fraction can be calculated theoretically or experimentally. This value was measured experimentally and can be seen in **Figure 29**. The linear fit was performed to the inverse of Kerr constant ($\Delta n/E^2$) as a function of volume fraction, ϕ. The dashed line is representation[88] of

$$\Delta n = \Delta n_{sat} \phi S_2$$

In this case, Δn_{sat} is the specific birefringence with a different notation. This yields to ϕ^* = 0.0179. This is the critical volume fraction for small platelets that represents the metastable limit in the isotropic phase.

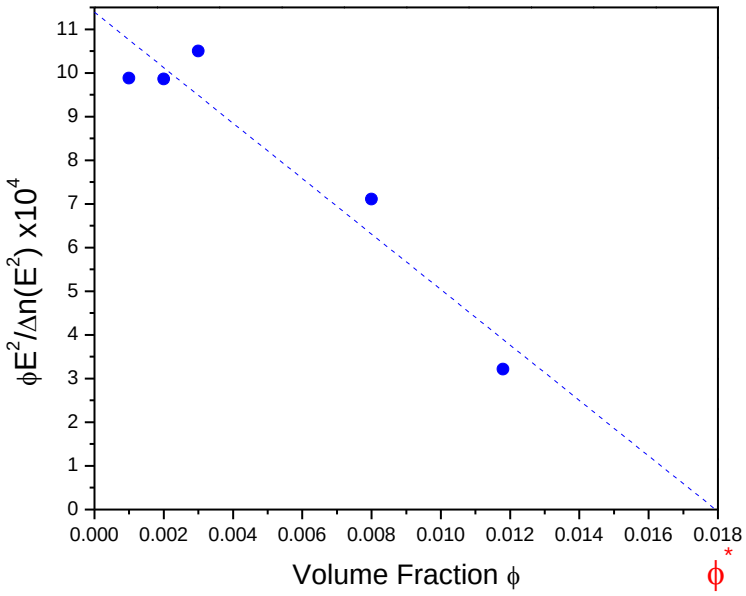

Figure 29. Another representation of induced birefringence of an isotropic suspension versus volume fraction. The spinodal volume fraction is when the linear birefringence approaches to zero.

As mentioned before, the biphasic region for small platelets lies in the range of $1.18\text{x}10^{-2} < \phi < 1.77\text{x}10^{-2}$; thus, from the obtained critical concentration, ϕ^* is close to the nematic region at coexistence.

The focus of this study is to test polarization to very diluted suspensions, for example, ($\phi \rightarrow 0$). For this case, the anisotropy of polarizability can be rewritten as

$$\Delta\alpha = -\frac{\Delta n}{E^2}\frac{15k_BT}{\Delta n^P}\left(\frac{1}{\phi}\right)$$

since $\phi/\phi^* \ll 1$.

Now that an equation for anisotropy of polarizability has been established and all the important parameters has been found, the measurements can now be made as shown in **Table 7** and **Table 8**.

System	ζ^{-1}	ϕ	I (mol/L)	$\Delta\alpha\ (J/E^2)$	κ (nm)
α-ZrP	901	0.1%	1.251×10^{-3}	$-4.499 \pm 0.472\times10^{-28}$	8.45 ± 0.015
	290	0.1%	1.41×10^{-3}	$-4.412 \pm 0.1698\times10^{-28}$	7.945 ± 0.008
	901	0.2%	2.384×10^{-3}	$-8.651 \pm 0.907\times10^{-28}$	6.12 ± 0.01
	290	0.2%	2.688×10^{-3}	$-4.533 \pm 0.174\times10^{-28}$	5.754 ± 0.01
	901	0.3%	3.584×10^{-3}	$-9.289 \pm 0.974\times10^{-28}$	4.99 ± 0.0066
	290	0.3%	3.872×10^{-3}	$-4.735 \pm 0.182\times10^{-28}$	4.794 ± 0.009

Table 7. Measurements of anisotropy of polarizability with changes of aspect ratio, volume, and ionic strength. Data for the effect of electric double layer, Debye length is also provided.

System	ζ^{-1}	ϕ	I (mol/L)	$\Delta\alpha\ (^{J}/_{E^2})$	κ (nm)
α-ZrP + 1mM TBACl	901	0.1%	2.352×10^{-3}	$-4.278 \pm 0.492\times10^{-28}$	6.16 ± 0.0084
	290	0.1%	2.48×10^{-3}	$-3.894 \pm 0.215\times10^{-28}$	6.00 ± 0.002
	901	0.2%	3.504×10^{-3}	$-4.413 \pm 0.508\times10^{-28}$	5.05 ± 0.01
	290	0.2%	3.76×10^{-3}	$-4.098 \pm 0.244\times10^{-29}$	4.88 ± 0.014
	901	0.3%	4.672×10^{-3}	$-6.382 \pm 0.734\times10^{-28}$	4.37 ± 0.005
	290	0.3%	4.928×10^{-3}	$-4.262 \pm 0.264\times10^{-28}$	4.25 ± 0.009

Table 8. Measurements of anisotropy of polarizability with changes of aspect ratio, volume, and ionic strength. Data for the effect of electric double layer, Debye length is also provided. This is when 1 mM TBACl is added to the suspension.

This confirms the effect in polarizability as changes in volume fraction, ionic strength, and aspect ratio occur. All measurements were done with the same solvent, Milli-Q water, and at the same temperature (room temperature).

The Debye length and Δα are plotted in **Figure 30** and **Figure 31** for better visualization. The addition of salt increases the ionic strength but decreases the double layer thickness. As a result, it decreases the sensitivity of the platelets to an electric field. Therefore, the anisotropy decreases due to the increase of both electrolyte conductivity and interflake interactions. This also induces a decrease in electric potential. In the isotropic phase, there is no specific d-spacing between particle to particle due to the random orientation. However, as an electric field is applied to the suspension, the

platelets get oriented and the particle to particle distance can be measured using 1-D SAXS.

In conclusion, the anisotropy value zirconium phosphate platelets are smaller compared to graphene oxide but is larger than gibbsite, montmorillonite, and beidellite particles.

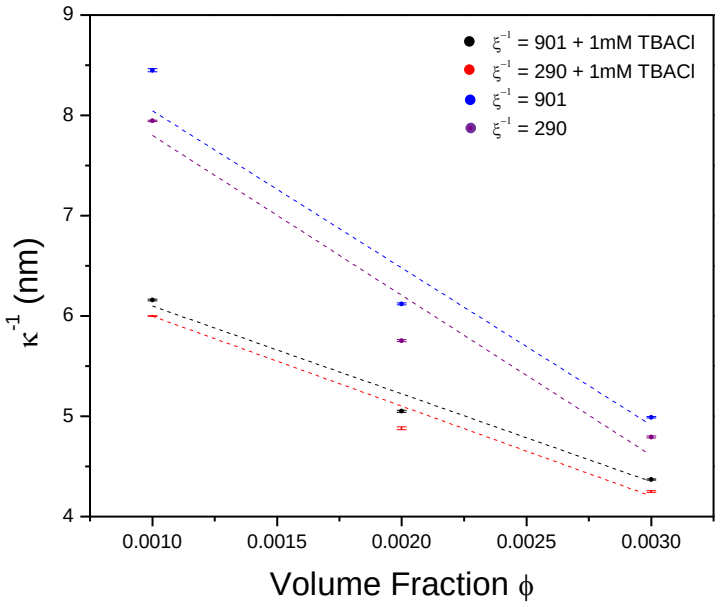

Figure 30. The Debye length is plotted as a function of volume fraction of two different aspect ratios when 1 mM of TBACl salt is added into the solution and when no salt is added, as indicated in the legend.

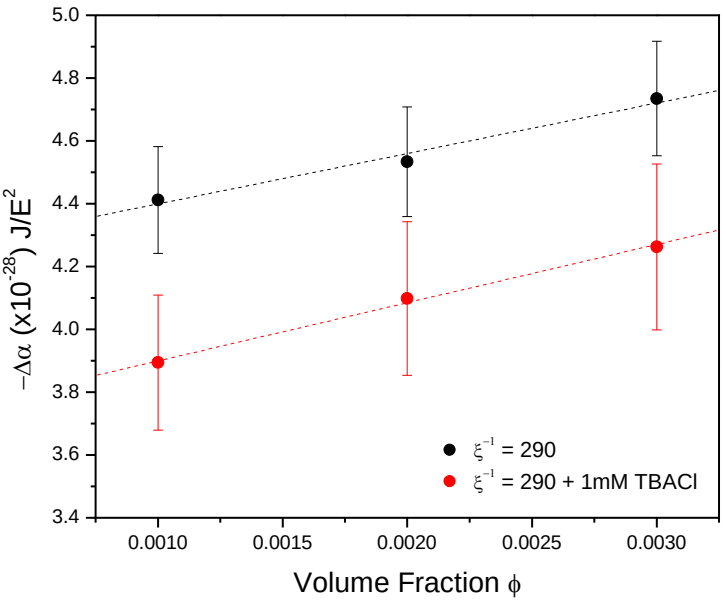

Figure 31. Effect in the polarizability of anisotropy in increasing volume fraction when one solution has salt and the other does not. The data points are in the isotropic region.

To make sure if the calculation of Δα are correct, the experimental result should match the theoretical result. This can be verified by using the equations derived in the **Theory of Anisotropy of Polarizability** section. In order to theoretically calculate Δα, the following values are needed: surface conductivity of zirconium phosphate, dielectric constant of the solvent, dielectric constant of zirconium phosphate[89], thickness and diameter of the platelet, conductivity of the solvent. For this case, the platelet of ϕ = 0.001 and $\zeta^{-1} = 901$ will be used for comparison.

The following values were obtained:

$$\alpha_{\parallel}^{\infty} = -9.12611\times10^{-29} F\cdot m^2$$

$$\alpha_{\perp}^{\infty} = -4.74826\times10^{-30} F\cdot m^2$$

$$\tau_{\perp} = 7.5971\times10^{-6} s$$

$$\tau_{\parallel} = 1.6584\times10^{-7} s$$

$$\alpha_{\parallel}^{0} = 4.8733\times10^{-30} F\cdot m^2$$

$$\alpha_{\perp}^{0} = 5.3738\times10^{-27} F\cdot m^2$$

Substituting each value to this equation,

$$\alpha_{\parallel,\perp} = \alpha_{\parallel,\perp}^{\infty} + \frac{\alpha_{\parallel,\perp}^{0} - \alpha_{\parallel,\perp}^{\infty}}{1+\omega^2\tau_{\parallel,\perp}^2}$$

$$\alpha = \alpha_{\parallel} - \alpha_{\perp} = -3.3620\times10^{-28}\frac{J}{E^2}$$

From **Table 7**, the experimental anisotropy of polarizability for large platelet at ϕ = 0.001, $\Delta\alpha = -4.499 \pm 0.472\times10^{-28}$. Even though this value is slightly higher than the theoretical value, both are of the same order of magnitude. Therefore, both the experimental and theoretical are in good agreement.

A visual representation is shown in **Figure 32**, where the blue line is the theoretical values of anisotropy for different aspect ratio. The anisotropy of polarization, $\Delta\alpha$, increases proportional to an increase in aspect ratio.

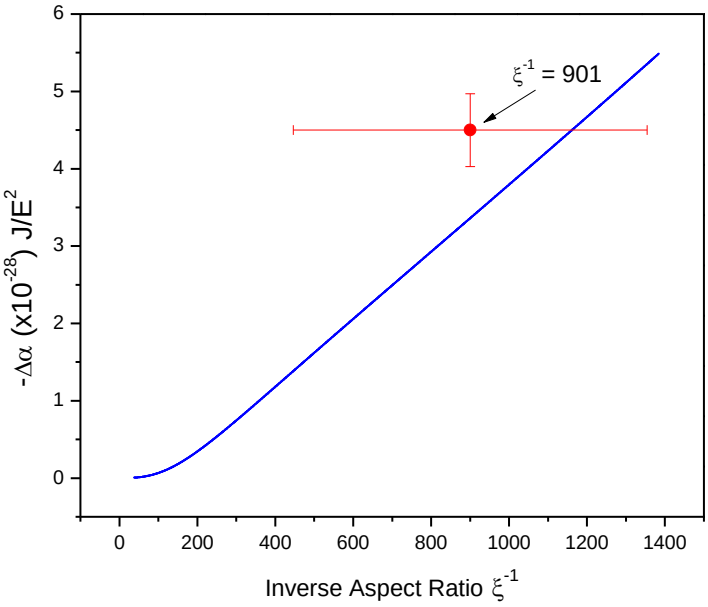

Figure 32. The solid lines are a representation of the theoretical MWO model as a function of aspect ratio for α-ZrP platelets when no extra salt is added. The dotted points are the experimental values of anisotropy of polarizability for very diluted suspensions. Since the platelets are polydisperse, error bars are included.

Kerr Coefficient

The Kerr coefficient as a function of frequency was obtained for two different aspect ratios at the same ionic strength and volume fractions. This was measured by using the EBS technique, with an α angle of 22°, and the sample was loaded in a Kerr cell.

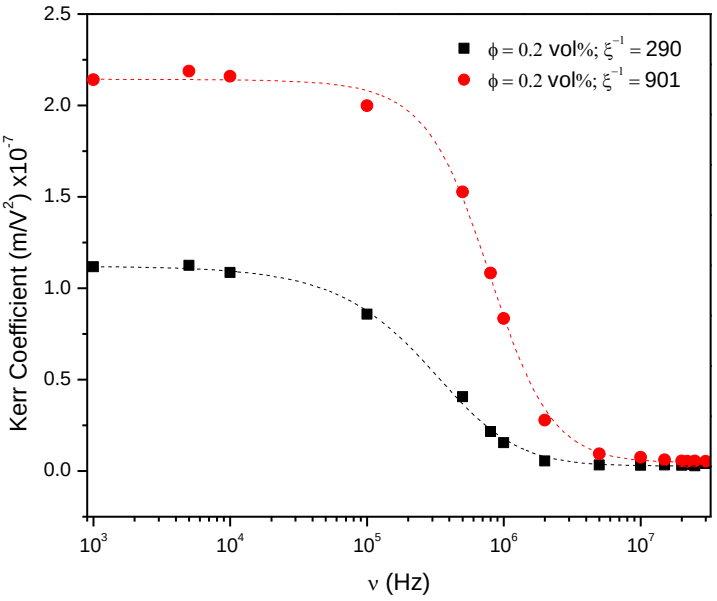

Figure 33. Frequency dependence of Kerr constant measured at two different aspect ratio nanoplates with same ionic strength. The continuous line is the best representation of EMW-2 model.

From **Figure 33**, the following observations can be seen:

I The Kerr constant depends on the frequency of the applied frequency. As the frequency goes to infinity, the Kerr coefficient saturates to a non-zero value. This is in good agreement with other works[90-91].

II The value of the Kerr constant of the suspension decreases with aspect ratio. For small particles, the Kerr coefficient is smaller.

III At frequencies above 10 MHz, the Kerr coefficient becomes independent to the ionic strength and particle charge. In other words, ionic motions are negligible. In this region, the Kerr coefficient behavior is that of an uncharged particle suspended in a dielectric fluid.

IV The cutoff frequency is the minimum slope that the Kerr coefficient can be defined. The cutoff frequency happens before the small platelets compared to the large platelets.

The frequency domains are divided into two regions: electrokinetic regime (1 kHz < ν < 1 MHz) and Maxwell-Wagner regime (1 MHz < ν < 30 MHz).

In the electrokinetic regime, particles respond to the combination of both electric and viscous components in the torque. The hydrodynamic torque cannot be neglected[14, 92] and the electric torque gets complicated in the presence of polarization. There are also changes in ion densities and electric double layers that makes the measurement of polarizability way too complicated and only limited amount of information is available for this region. The Kerr coefficient is monotonically at the beginning and then it decreases smoothly for low charge particles. The Kerr coefficient does not depend much on the frequency for high charge particles[91].

In the Maxwell-Wagner regime, the Kerr coefficient decreases sharply to an asymptotic value 100 kHz to 30 MHz. This region changes depending on the size of the particle. For small platelets, the asymptotic value happened at lower frequency. In this

regime, it is easy to make observations because viscous forces and electric torque are not affected by the polarization[68, 93]. From the relaxation region (100 kHz < ν < 30 MHz), at the lower frequency, the particle starts to accumulate charges on both sides due to the conductivity mismatch between the surface and the solvent. At higher frequencies, the particles move so fast that conduction charges do not have enough time to move around and the remaining dipole coefficient from the particle is due to the permittivity mismatch between the surface of the particle and the solvent.

In conclusion, the spectrum is the result of the Maxwell-Wagner-O'Konski relaxation model.

CHAPTER V

SUMMARY AND CONCLUSIONS

Summary

Isotropic colloidal suspensions are of potential use for electronic devices. The Kerr coefficient of the system defines how good the system is for industrial applications. For this study, zirconium phosphate platelets were used and the Kerr coefficient was compared to other systems, such as graphene oxides, beidellite, and gibbsites to see their potential applications. Liquid crystal is a state of matter that exhibits properties of both solid and a liquid. One form of liquid crystal that was used for this study are lyotropic discotic liquid crystals whose phase depends on the concentration. α-zirconium phosphate has advantages over natural clays for its high ionic exchange and ease of intercalation and exfoliation. Also, α-zirconium phosphate are monodisperse, easy to control the size, and biodegradable. The α-zirconium phosphate platelets were synthesized using the hydrothermal method and then the platelets were exfoliated to break the plates into monolayers. Phase diagrams of the zirconium phosphate platelets were created to determine the region where the suspension becomes isotropic, biphasic, or nematic. The smaller platelets sediment faster than the larger platelets due to their faster rotational and translation rates. Birefringence is an optical property of the liquid crystal as they have refractive indexes that depends on the polarization of the incident light. Isotropic suspensions do not show any form of birefringence, unless the birefringence is induced. Isotropic suspension can show flow induced birefringence when the suspension is shaken. It can also show birefringence when an electric field is

applied. An application of electric field reorients the particles to have their director perpendicular to the field; thus, inducing some birefringence. The measurement of induced birefringence was both obtained by image analysis (not an accurate measurement) and by using an electro-optical measurement technique, Electric Birefringence Spectroscopy (EBS). The isotropic suspension was placed in a Kerr cell, where a light beam transverses through a polarizer, to the sample, to a quarter-wave plate, to an analyzer, and finally to a photodetector. All the measurements were extracted from an oscilloscope and the data was then converted into induced birefringence. The induced birefringence was then plotted as a function of the electric field squared where the following information was obtained: specific birefringence, Kerr coefficient, spinodal volume fraction, and the polarizability of the platelet. The spectrum of the zirconium phosphate platelets resulted from the Maxwell-Wagner-O'Konski relaxation. The induced-dipole moment decreased near the MHz region. The Kerr coefficient of zirconium phosphate is lower than graphene oxide but it is higher than gibbsite, beidellite, and montmorillonite particles.

Conclusions

We studied the field induced birefringence in the isotropic phase of zirconium phosphate particles with different aspect ratios of 901 and 290. There are no studies in the electric field effect of zirconium phosphate platelets, and we plan to fill-up in the literature missing information about their electro-optical properties. The samples were observed under the isotropic phase to see that the induced birefringence is dependent in volume fraction, size, and ionic strength. According to SAXS experiments, the particles saturates to an induced order parameter, $S^{sat} = -0.5$. This corresponds to a perfect 'anti-nematic' order of zirconium phosphate platelets. With the simple model of Electric Birefringence Spectroscopy, we showed that the anisotropy of polarizability of zirconium phosphate is in good agreement with the MWO polarization mechanism. We also showed that surface conductivity, as well as aspect ratio, plays a major role in the polarization. As the salt concentration increases in the suspension, the sensitivity of the electric field decreases due to conductive electrolytes and interflake interactions. As the inverse aspect ratio decreases, the polarizability also decreases. We concluded that our system follows the MWO relaxation, and both the theoretical and experimental polarizability were in good agreement to each other.

REFERENCES

[1] Demus, D.; Richter, L., *Textures of liquid crystals*. Deutscher Verlag für Grundstoffindustrie: 1980.

[2] Brinkman, W. F.; Cladis, P. E., Defects in liquid crystals. *Physics Today* **1982,** *35* (5), 48-54.

[3] Demus, D.; Goodby, J. W.; Gray, G. W.; Spiess, H. W.; Vill, V., *Handbook of liquid crystals, low molecular weight liquid crystals I: calamitic liquid crystals*. John Wiley & Sons: 2011.

[4] Chandrasekhar, S.; Sadashiva, B.; Suresh, K., Liquid crystals of disc-like molecules. *pramana* **1977,** *9* (5), 471-480.

[5] Lei, L., Bowlic Liquid Crystalsl. *Molecular Crystals and Liquid Crystals* **1987,** *146* (1), 41-54.

[6] Chandrasekhar, S.; Ranganath, G., The structure and energetics of defects in liquid crystals. *Advances in Physics* **1986,** *35* (6), 507-596.

[7] Billard, J.; Dubois, J.; Huutinh, N.; Zann, A., Mesophase of disc-like molecules. *NOUVEAU JOURNAL DE CHIMIE-NEW JOURNAL OF CHEMISTRY* **1978,** *2* (5), 535-540.

[8] van der Kooij, F. M.; Kassapidou, K.; Lekkerkerker, H. N., Liquid crystal phase transitions in suspensions of polydisperse plate-like particles. *Nature* **2000,** *406* (6798), 868-871.

[9] Nakato, T.; Nakamura, K.; Shimada, Y.; Shido, Y.; Houryu, T.; Iimura, Y.; Miyata, H., Electrooptic response of colloidal liquid crystals of inorganic oxide nanosheets prepared by exfoliation of a layered niobate. *The Journal of Physical Chemistry C* **2011,** *115* (18), 8934-8939.

[10] Shen, T.-Z.; Hong, S.-H.; Song, J.-K., Electro-optical switching of graphene oxide liquid crystals with an extremely large Kerr coefficient. *Nature materials* **2014,** *13* (4), 394-399.

[11] Shuai, M.; Mejia, A. F.; Chang, Y.-W.; Cheng, Z., Hydrothermal synthesis of layered α-zirconium phosphate disks: control of aspect ratio and polydispersity for nano-architecture. *CrystEngComm* **2013,** *15* (10), 1970-1977.

[12] Nguyen, V. H., Recent advances in experimental basic research on graphene and graphene-based nanostructures. *Advances in Natural Sciences: Nanoscience and Nanotechnology* **2016,** *7* (2), 023001.

[13] Singh, S.; Dunmur, D. A., *Liquid crystals: fundamentals*. World Scientific: 2002.

[14] Delgado, Á. V., *Interfacial electrokinetics and electrophoresis*. CRC Press: 2001; Vol. 106.

[15] Kerr, J., XL. A new relation between electricity and light: Dielectrified media birefringent. *The London, Edinburgh, and Dublin Philosophical Magazine and Journal of Science* **1875,** *50* (332), 337-348.

[16] Gerber, P. R., Electro-optical effects of a small-pitch blue-phase system. *Molecular Crystals and Liquid Crystals* **1985,** *116* (3-4), 197-206.

[17] Jiménez, M. L.; Fornasari, L.; Mantegazza, F.; Mourad, M. C.; Bellini, T., Electric birefringence of dispersions of platelets. *Langmuir* **2011,** *28* (1), 251-258.

[18] Arenas-Guerrero, P.; Iglesias, G. R.; Delgado, Á. V.; Jiménez, M. L., Electric birefringence spectroscopy of montmorillonite particles. *Soft matter* **2016,** *12* (22), 4923-4931.

[19] Hong, S.-H.; Shen, T.-Z.; Song, J.-K., Electro-optical characteristics of aqueous graphene oxide dispersion depending on ion concentration. *The Journal of Physical Chemistry C* **2014,** *118* (45), 26304-26312.

[20] Yan, J.; Jiao, M.; Rao, L.; Wu, S.-T., Direct measurement of electric-field-induced birefringence in a polymer-stabilized blue-phase liquid crystal composite. *Optics express* **2010,** *18* (11), 11450-11455.

[21] Davidson, P.; Gabriel, J.-C. P., Mineral liquid crystals. *Current opinion in colloid & interface science* **2005,** *9* (6), 377-383.

[22] Sun, D.; Sue, H.-J.; Cheng, Z.; Martínez-Ratón, Y.; Velasco, E., Stable smectic phase in suspensions of polydisperse colloidal platelets with identical thickness. *Physical Review E* **2009,** *80* (4), 041704.

[23] Chang, Y.-W.; Mejia, A. F.; Cheng, Z.; Di, X.; McKenna, G. B., Gelation via Ion Exchange in Discotic Suspensions. *Physical review letters* **2012,** *108* (24), 247802.

[24] Yang, F.; Liu, S.; Xu, J.; Lan, Q.; Wei, F.; Sun, D., Pickering emulsions stabilized solely by layered double hydroxides particles: The effect of salt on emulsion formation and stability. *Journal of Colloid and Interface Science* **2006,** *302* (1), 159-169.

[25] Bon, S. A.; Colver, P. J., Pickering miniemulsion polymerization using laponite clay as a stabilizer. *Langmuir* **2007,** *23* (16), 8316-8322.

[26] Ashby, N.; Binks, B., Pickering emulsions stabilised by Laponite clay particles. *Physical Chemistry Chemical Physics* **2000,** *2* (24), 5640-5646.

[27] Cavallo, F.; Lagally, M. G., Semiconductors turn soft: inorganic nanomembranes. *Soft Matter* **2010,** *6* (3), 439-455.

[28] Harnau, L., Structure and thermodynamics of platelet dispersions. *Molecular Physics* **2008,** *106* (16-18), 1975-2000.

[29] Mejia, A. F.; Chang, Y.-W.; Ng, R.; Shuai, M.; Mannan, M. S.; Cheng, Z., Aspect ratio and polydispersity dependence of isotropic-nematic transition in discotic suspensions. *Physical Review E* **2012,** *85* (6), 061708.

[30] Bates, M. A.; Frenkel, D., Influence of polydispersity on the phase behavior of colloidal liquid crystals: A Monte Carlo simulation study. *The Journal of chemical physics* **1998,** *109* (14), 6193-6199.

[31] Gura, V.; Macy, A. S.; Beizai, M.; Ezon, C.; Golper, T. A., Technical breakthroughs in the wearable artificial kidney (WAK). *Clinical Journal of the American Society of Nephrology* **2009,** *4* (9), 1441-1448.

[32] Bauer, F.; Willert-Porada, M., Microstructural characterization of Zr-phosphate–Nafion® membranes for direct methanol fuel cell (DMFC) applications. *Journal of Membrane Science* **2004,** *233* (1), 141-149.

[33] Alberti, G., Syntheses, crystalline structure, and ion-exchange properties of insoluble acid salts of tetravalent metals and their salt forms. *Acc. Chem. Res.;(United States)* **1978,** *11* (4).

[34] Clearfield, A.; Stynes, J., The preparation of crystalline zirconium phosphate and some observations on its ion exchange behaviour. *Journal of Inorganic and Nuclear Chemistry* **1964,** *26* (1), 117-129.

[35] Yu, Y.-H.; Wang, X.; Shinde, A.; Cheng, Z., Synthesis and Exfoliation of Discotic Zirconium Phosphates to Obtain Colloidal Liquid Crystals. *JoVE (Journal of Visualized Experiments)* **2016,** (111), e53511-e53511.

[36] Yu, Y.-H.; Chen, Y.-P.; Cheng, Z., Microwave-assisted synthesis of rod-like CuO/TiO 2 for high-efficiency photocatalytic hydrogen evolution. *International Journal of Hydrogen Energy* **2015,** *40* (46), 15994-16000.

[37] Alberti, G.; Casciola, M.; Costantino, U.; Levi, G.; Ricciardi, G., On the mechanism of diffusion and ionic transport in crystalline insoluble acid salts of tetravalent metals—I Electrical conductance of zirconium bis (monohydrogen ortho-phosphate) monohydrate with a layered structure. *Journal of Inorganic and Nuclear Chemistry* **1978,** *40* (3), 533-537.

[38] Kraus, K. A.; Phillips, H. O., ADSORPTION ON INORGANIC MATERIALS. I. CATION EXCHANGE PROPERTIES OF ZIRCONIUM PHOSPHATE1. *Journal of the American Chemical Society* **1956,** *78* (3), 694-694.

[39] Sun, L.; Boo, W. J.; Sun, D.; Clearfield, A.; Sue, H.-J., Preparation of exfoliated epoxy/α-zirconium phosphate nanocomposites containing high aspect ratio nanoplatelets. *Chemistry of Materials* **2007,** *19* (7), 1749-1754.

[40] Sun, X.; Luo, D.; Liu, J.; Evans, D. G., Monodisperse chemically modified graphene obtained by density gradient ultracentrifugal rate separation. *Acs Nano* **2010,** *4* (6), 3381-3389.

[41] Kim, H.-N.; Keller, S. W.; Mallouk, T. E.; Schmitt, J.; Decher, G., Characterization of zirconium phosphate/polycation thin films grown by sequential adsorption reactions. *Chemistry of Materials* **1997,** *9* (6), 1414-1421.

[42] He, P.; Mejia, A. F.; Cheng, Z.; Sun, D.; Sue, H.-J.; Dinair, D. S.; Marquez, M., Hindrance function for sedimentation and creaming of colloidal disks. *Physical Review E* **2010,** *81* (2), 026310.

[43] Lekkerkerker, H. N. W.; Coulon, P.; Van Der Haegen, R.; Deblieck, R., On the isotropic-liquid crystal phase separation in a solution of rodlike particles of different lengths. *The Journal of chemical physics* **1984,** *80* (7), 3427-3433.

[44] Wensink, H.; Lekkerkerker, H., Phase diagram of hard colloidal platelets: a theoretical account. *Molecular Physics* **2009,** *107* (20), 2111-2118.

[45] Onsager, L., The effects of shape on the interaction of colloidal particles. *Annals of the New York Academy of Sciences* **1949,** *51* (4), 627-659.

[46] Oswald, P.; Pieranski, P., *Nematic and cholesteric liquid crystals: concepts and physical properties illustrated by experiments*. CRC press: 2005.

[47] Oswald, P.; Pieranski, P., *Smectic and columnar liquid crystals: concepts and physical properties illustrated by experiments*. CRC Press: 2005.

[48] Drzaic, P. S., *Liquid crystal dispersions*. World Scientific: 1995; Vol. 1.

[49] Verhoeff, A.; Bakelaar, I.; Otten, R.; van der Schoot, P.; Lekkerkerker, H., Tactoids of plate-like particles: Size, shape, and director field. *Langmuir* **2010,** *27* (1), 116-125.

[50] Shinde, A.; Wang, X.; Cheng, Z., Aspect Ratio Dependence of Isotropic-Nematic Phase Separation of Nanoplates in Gravity. *Gravitational and Space Research* **2016,** *4* (1).

[51] O'KONSKI, C. T.; Zimm, B. H., New method for studying electrical orientation and relaxation effects in aqueous colloids; preliminary results with tobacco mosaic virus. *Science (New York, NY)* **1950,** *111* (2875), 113-116.

[52] Buka, A.; Kramer, L., *Pattern formation in liquid crystals*. Springer Science & Business Media: 2012.

[53] Prost, J., *The physics of liquid crystals*. Oxford university press: 1995.

[54] Clark, N.; Handschy, M.; Lagerwall, S., Ferroelectric liquid crystal electro-optics using the surface stabilized structure. *Molecular Crystals and Liquid Crystals* **1983,** *94* (1-2), 213-233.

[55] Taylor, T.; Fergason, J.; Arora, S., Biaxial liquid crystals. *Physical Review Letters* **1970,** *24* (8), 359.

[56] Lemaire, B. J.; Davidson, P.; Ferré, J.; Jamet, J.-P.; Petermann, D.; Panine, P.; Dozov, I.; Stoenescu, D.; Jolivet, J.-P., The complex phase behaviour of suspensions of goethite (α-FeOOH) nanorods in a magnetic field. *Faraday discussions* **2005,** *128*, 271-283.

[57] Dozov, I.; Paineau, E.; Davidson, P.; Antonova, K.; Baravian, C.; Bihannic, I.; Michot, L., Electric-field-induced perfect anti-nematic order in isotropic aqueous suspensions of a natural beidellite clay. *The Journal of Physical Chemistry B* **2011,** *115* (24), 7751-7765.

[58] op Reinink, A. L.; van den Pol, E.; Petukhov, A.; Vroege, G.; Lekkerkerker, H., Phase behaviour of lyotropic liquid crystals in external fields and confinement. *The European Physical Journal Special Topics* **2013,** *222* (11), 3053-3069.

[59] Kim, J. E.; Han, T. H.; Lee, S. H.; Kim, J. Y.; Ahn, C. W.; Yun, J. M.; Kim, S. O., Graphene oxide liquid crystals. *Angewandte Chemie International Edition* **2011,** *50* (13), 3043-3047.

[60] Houssier, C.; O'Konski, C. T., Electro-optical instrumentation systems with their data acquisition and treatment. In *Molecular Electro-Optics*, Springer: 1981; pp 309-339.

[61] Hong, S.-H.; Shen, T.-Z.; Song, J.-K., Flow-induced alignment of disk-like graphene oxide particles in isotropic and biphasic colloids. *Molecular Crystals and Liquid Crystals* **2015,** *610* (1), 68-76.

[62] Yariv, A.; Yeh, P., *Optical waves in crystals*. Wiley, New York: 1984; Vol. 10.

[63] Yeh, P., Extended Jones matrix method. *JOSA* **1982,** *72* (4), 507-513.

[64] Gu, C.; Yeh, P., Extended Jones matrix method. II. *JOSA A* **1993,** *10* (5), 966-973.

[65] Piazza, R.; Degiorgio, V.; Bellini, T., Matrix analysis of electric birefringence measurements. *Optics communications* **1986,** *58* (6), 400-404.

[66] Wu, S.-T.; Efron, U.; Hess, L. D., Birefringence measurements of liquid crystals. *Applied optics* **1984,** *23* (21), 3911-3915.

[67] Fredericq, E.; Houssier, C., Electric dichroism and electric birefringence. **1973**.

[68] Saville, D.; Bellini, T.; Degiorgio, V.; Mantegazza, F., An extended Maxwell–Wagner theory for the electric birefringence of charged colloids. *The Journal of Chemical Physics* **2000,** *113* (16), 6974-6983.

[69] Delgado, A.; Carrique, F.; Arroyo, F.; Bellini, T.; Mantegazza, F.; Giardini, M. E.; Degiorgio, V., Frequency dependence of the dielectric and electro-optic response in suspensions of charged rod-like colloidal particles. *Colloids and Surfaces A: Physicochemical and Engineering Aspects* **1998,** *140* (1), 157-167.

[70] O'Konski, C. T.; Yoshioka, K.; Orttung, W. H., Electric properties of macromolecules. IV. Determination of electric and optical parameters from saturation of electric birefringence in solutions. *The Journal of Physical Chemistry* **1959,** *63* (10), 1558-1565.

[71] Bragg, W. L.; Pippard, A. B., The form birefringence of macromolecules. *Acta Crystallographica* **1953,** *6* (11-12), 865-867.

[72] de La Cotte, A.; Merzeau, P.; Kim, J. W.; Lahlil, K.; Boilot, J.-P.; Gacoin, T.; Grelet, E., Electric field induced birefringence in non-aqueous dispersions of mineral nanorods. *Soft matter* **2015,** *11* (33), 6595-6603.

[73] Thurston, G.; Bowling, D., The frequency dependence of the Kerr effect for suspensions of rigid particles. *Journal of Colloid and Interface Science* **1969,** *30* (1), 34-45.

[74] O'konski, C.; Haltner, A., Electric Properties of Macromolecules. I. A Study of Electric Polarization in Polyelectrolyte Solutions by Means of Electric Birefringence1. *Journal of the American Chemical Society* **1957,** *79* (21), 5634-5649.

[75] Edwards, M.; Wu, X.; Wu, J.-S.; Huang, J.; Kellay, H., Electric-field effects on a droplet microemulsion. *Physical Review E* **1998,** *57* (1), 797.

[76] Maxwell, J., Electricity and Magnetism, v. 1. *Clarendon, Oxford* **1892**, 452.

[77] Wagner, K., Explanation of Dielectric Polarization Proc-c~ ses on the Basis of Maxwellian Concepts. *Arch. Electrotech* **1914,** *2* (9), 371-87.

[78] Zijlstra, P.; van Stee, M.; Verhart, N.; Gu, Z.; Orrit, M., Rotational diffusion and alignment of short gold nanorods in an external electric field. *Physical Chemistry Chemical Physics* **2012,** *14* (13), 4584-4588.

[79] Grosse, C.; Pedrosa, S.; Shilov, V. N., Calculation of the dielectric increment and characteristic time of the LFDD in colloidal suspensions of spheroidal particles. *Journal of colloid and interface science* **1999,** *220* (1), 31-41.

[80] Stratton, J., Electromagnetic Theory, McGraw-Hill, New York, 1941. *There is no corresponding record for this reference* **1993**.

[81] O'Konski, C. T., Electric properties of macromolecules. V. Theory of ionic polarization in polyelectrolytes. *The Journal of Physical Chemistry* **1960,** *64* (5), 605-619.

[82] Hunter, R., Electrified interfaces: the electrical double layer. *Foundations of Colloid Science* **2001**, 317-325.

[83] Konkena, B.; Vasudevan, S., Understanding aqueous dispersibility of graphene oxide and reduced graphene oxide through p K a measurements. *The journal of physical chemistry letters* **2012,** *3* (7), 867-872.

[84] Van der Beek, D.; Petukhov, A.; Davidson, P.; Ferré, J.; Jamet, J.; Wensink, H.; Vroege, G.; Bras, W.; Lekkerkerker, H., Magnetic-field-induced orientational order in the isotropic phase of hard colloidal platelets. *Physical Review E* **2006,** *73* (4), 041402.

[85] Fraden, S.; Maret, G.; Caspar, D.; Meyer, R. B., Isotropic-nematic phase transition and angular correlations in isotropic suspensions of tobacco mosaic virus. *Physical review letters* **1989,** *63* (19), 2068.

[86] Stroobants, A.; Lekkerkerker, H.; Odijk, T., Effect of electrostatic interaction on the liquid crystal phase transition in solutions of rodlike polyelectrolytes. *Macromolecules* **1986,** *19* (8), 2232-2238.

[87] Fixman, M.; Skolnick, J., Polyelectrolyte excluded volume paradox. *Macromolecules* **1978,** *11* (5), 863-867.

[88] Lemaire, B.; Davidson, P.; Ferré, J.; Jamet, J.; Petermann, D.; Panine, P.; Dozov, I.; Jolivet, J., Physical properties of aqueous suspensions of goethite (-FeOOH) nanorods Part I: In the isotropic phase. *The European Physical Journal E: Soft Matter and Biological Physics* **2004,** *13* (3), 291-308.

[89] Casciola, M.; Constantino, U.; Fazzini, S.; Tosoratti, G., Dielectric properties of α-zirconium phosphate and its organic derivatives. *Solid State Ionics* **1983,** *8* (1), 27-34.

[90] Mantegazza, F.; Bellini, T.; Degiorgio, V.; Delgado, A. V.; Arroyo, F. J., Electrokinetic properties of colloids of variable charge. II. Electric birefringence versus dielectric properties. *The Journal of chemical physics* **1998,** *109* (16), 6905-6910.

[91] Mantegazza, F.; Bellini, T.; Buscaglia, M.; Degiorgio, V.; Saville, D., Electrokinetic properties of colloids of variable charge. III. Observation of a Maxwell–Wagner relaxation mechanism by high-frequency electric-birefringence spectroscopy. *The Journal of Chemical Physics* **2000,** *113* (16), 6984-6991.

[92] Teubner, M., The motion of charged colloidal particles in electric fields. *The Journal of Chemical Physics* **1982,** *76* (11), 5564-5573.

[93] Dukhin, S. S.; Shilov, V. N.; Bikerman, J., Dielectric phenomena and double layer in disperse systems and polyelectrolytes. *Journal of the Electrochemical Society* **1974,** *121* (4), 154C-154C.